Department of Applied Physics

Interferometric methods for aberration-insensitive imaging and generation of light beams with controlled group velocity

Elena Ilina

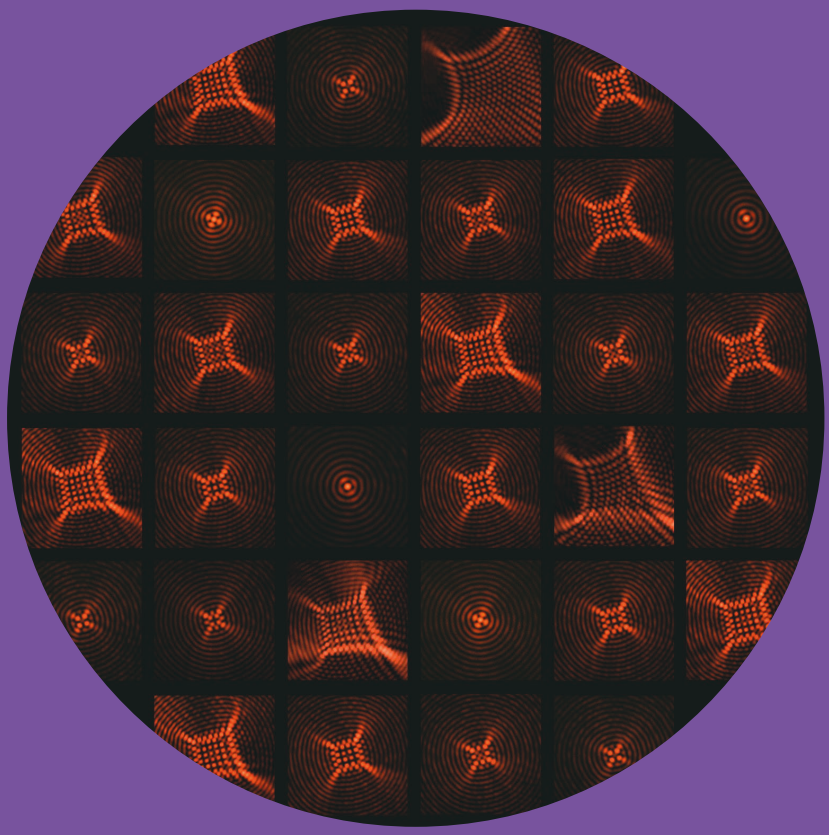

Aalto University

DOCTORAL THESES

Aalto University publication series
DOCTORAL THESES 32/2023

Interferometric methods for aberration-insensitive imaging and generation of light beams with controlled group velocity

Elena Ilina

A doctoral thesis completed for the degree of Doctor of Science (Technology) to be defended, with the permission of the Aalto University School of Science, at a public examination held at the lecture hall AS1 of the TUAS building (Maarintie 8, Espoo, Finland) on 24th of March 2023 at 12.00.

Aalto University
School of Science
Department of Applied Physics
Optics and Photonics group

Supervising professor
Professor Päivi Törmä, Aalto University, Finland

Thesis advisor
Dr. Andriy Shevchenko, Aalto University, Finland

Preliminary examiners
Professor Klas Lindfors, University of Cologne, Germany
Assistant Professor Marco Ornigotti, Tampere University, Finland

Opponent
Asistant Professor Marc Guillon, University of Paris, France

Aalto University publication series
DOCTORAL THESES 32/2023

ISBN 978-952-64-1176-7 (printed)
ISBN 978-952-64-1177-4 (pdf)
ISSN 1799-4934 (printed)
ISSN 1799-4942 (pdf)
http://urn.fi/URN:ISBN:978-952-64-1177-4

Unigrafia Oy
Helsinki 2023

Finland

NORDIC SWAN ECOLABEL
Printed matter
4041-0619

Aalto University

Abstract

Aalto University, P.O. Box 11000, FI-00076 Aalto www.aalto.fi

Author
Elena Ilina

Name of the doctoral thesis
Interferometric methods for aberration-insensitive imaging and generation of light beams with controlled group velocity

Publisher School of Science

Unit Department of Applied Physics

Series Aalto University publication series DOCTORAL THESES 32/2023

Field of research Optics, Photonics

Manuscript submitted 13 December 2022 **Date of the defence** 24 March 2023

Permission for public defence granted (date) 2 February 2023 **Language** English

☐ **Monograph** ☒ **Article thesis** ☐ **Essay thesis**

Abstract

Optical interferometry has many important applications in science and technology. For example, it is used to improve the performance of interferometric imaging systems, to detect weak signals in cosmology, to measure surface profiles and vibrations in metrology, and to visualize the amplitude and phase profiles of optical fields in holography.

The main goal of the research presented in this thesis is to study static and dynamic interference effects and use them to develop novel methods for optical imaging and detection, as well as to create new structured optical beams with controlled group velocity in free space.

A variety of imaging systems utilizing the intensity or field correlations of light have in the past few decades significantly extended their range of applications towards non-invasive scanning of three-dimensional objects and imaging through turbid media. However, the existing techniques are often not robust and have a relatively low resolution. In the thesis, we introduce novel interferometric imaging systems that combine the advantages of optical coherence tomography and classical ghost imaging to exhibit a high transverse resolution and insensitivity to optical aberrations. These systems are able to reveal a sharp image of the object even if its intensity image is completely destroyed by aberrations. The method can be used in optical microscopy, endoscopy, and three-dimensional imaging systems.

The thesis also describes a method to create non-diverging multifrequency optical beams with controlled group velocity in free space. These beams exhibit the wave beating phenomenon, and the control of the group velocity in them is based on dynamic interference effects. We show that by adjusting the angular dispersion of the beam's plane-wave components, essentially arbitrary values of the group velocity can be achieved. We demonstrate theoretically that continuous-wave and pulsed Bessel beams with superluminal, subluminal and negative group velocities can be created. Furthermore, we find that the on-axis group velocity of a beam can be a function of both spatial and temporal coordinates. We demonstrate experimentally a longitudinally accelerating optical beam that shows both negative and positive group velocities with a magnitude several times higher than the speed of light in vacuum. The fact that the group velocity of the beam depends on the on-axis phase distribution of its frequency components allows one to measure the local group velocity interferometrically. The measured group velocities in the conducted experiments agree well with the theoretical predictions. Such optical beams can find applications in intensity interferometry, ultrafast optics, optical tweezers, and nonlinear optics.

Keywords Optical imaging, coherence, interferometry, structured beams

ISBN (printed) 978-952-64-1176-7 **ISBN (pdf)** 978-952-64-1177-4

ISSN (printed) 1799-4934 **ISSN (pdf)** 1799-4942

Location of publisher Helsinki **Location of printing** Helsinki **Year** 2023

Pages 102 **urn** http://urn.fi/URN:ISBN:978-952-64-1177-4

Preface

The doctoral studies concluded by this dissertation were carried out in the Optics and Photonics group at the Department of Applied Physics of Aalto University. It has been a journey of personal and academic growth, and I wish to express my gratitude for the support and guidance I have received along the way.

First, I would like to acknowledge my Supervising Professor Matti Kaivola and Thesis Advisor Dr. Andriy Shevchenko. Their unwavering support and encouragement have been invaluable, and without their guidance, this dissertation would not have been possible. In addition, I am grateful to Professor Päivi Törmä for her help with the preparation of the documents required for the thesis publication.

I appreciate the time and efforts that Professor Klas Lindfors from University of Cologne and Assistant Professor Marco Ornigotti from Tampere University have invested in careful pre-examination of the thesis. In advance, I want to thank Assistant Professor Marc Guillon from University of Paris for acting as an opponent in the defense.

It is important for me to mention also other members of our research group, especially Dr. Markus Nyman, Somendu Maurya, Panu Hildén, Dr. Sushmita Paul, Dr. Radoslaw Kolkowski, and Evgeniia Ponomareva together with other colleagues from the School of Science and Micronova building. Collaborating with them has been a great learning experience and a source of inspiration, and I am grateful for the time we spent together. Special thanks go to my wonderful new colleagues from Dispelix for cheering me up during the last year of my studies when I was writing the thesis.

Last but not least, my sincere gratitude goes to my dear parents Viktoriia and Aleksandr, my darling husband Oleg, and our close friends for their love and unconditional support that kept me motivated during this challenging journey.

The work has been financed by the Academy of Finland and personal grants from Walter Ahlström foundation, Sähköinsinööriliiton Säätiö (SIL), and Tietotekniikan ja Elektroniikan Seura (TiES).

Espoo, February 20, 2023,

Elena Ilina

Contents

List of Publications

This thesis consists of an overview and of the following publications which are referred to in the text by their Roman numerals.

I E. Ilina, M. Nyman, I. Švagždytė, N. Chekurov, M. Kaivola, T. Setälä and A. Shevchenko. Aberration-insensitive microscopy using optical field-correlation imaging. *APL Photonics*, 4, 066102, June 2019.

II E. Ilina, M. Nyman, T. Mondal, M. Kaivola, T. Setälä, and A. Shevchenko. Interferometric imaging of reflective micro-objects in the presence of strong aberrations. *Optics Express*, 28, 1817-1826, January 2020.

III P. Hildén, E. Ilina, M. Kaivola, and A. Shevchenko. Multifrequency Bessel beams with adjustable group velocity and longitudinal acceleration in free space. *New Journal of Physics*, 24, 033042, March 2022.

IV E. Ilina, P. Hildén, M. Kaivola, and A. Shevchenko. Continuous-wave Bessel beams with strong longitudinal acceleration in free space. *Optics Letters*, 47, 4060-4063, August 2022.

Author's Contribution

Publication I: "Aberration-insensitive microscopy using optical field-correlation imaging"

DC constructed the setup and conducted the experiments, MN and IŠ built the first experimental setup, NC fabricated the samples, MK supervised the research, TS and AS developed the theory, DC wrote the article with contributions from the other authors.

Publication II: "Interferometric imaging of reflective micro-objects in the presence of strong aberrations"

DC constructed the experimental setup with contribution from MN and TM, DC conducted the experiments, MK supervised the research, TS and AS developed the theory, DC wrote the article with contributions from the other authors.

Publication III: "Multifrequency Bessel beams with adjustable group velocity and longitudinal acceleration in free space"

PH, DC and AS developed the theory, DC contributed to the theoretical description of accelerating two-component Bessel beams and the interpretation of the obtained results, MK supervised the research, PH wrote the article with contributions from the other authors.

Publication IV: "Continuous-wave Bessel beams with strong longitudinal acceleration in free space"

DC constructed the experimental setup and conducted the experiments, PH participated in the experiments, MK supervised the research, AS developed the theory, DC wrote the article with contributions from the other authors.

1. Introduction

Light emitted by a thermal source is a superposition of uncorrelated optical waves radiated independently by different atoms and/or molecules of the source. The amplitude and phase of such light are random functions of time and space characterized by means of statistical optics. The concepts of temporal and spatial coherence of light are used for this purpose. In contrast to monochromatic light, which is fully coherent, the aforementioned thermal light has a large bandwidth and is essentially temporally incoherent. Since thermal sources are spatially extended, their radiation in the vicinity of the source is also spatially incoherent. In general, any light is partially coherent, combining the random and deterministic characteristics that can be used for a variety of scientific and technological applications [1]. For example, highly coherent light is widely used in interferometry [2, 3, 4, 5], while incoherent or partially coherent light finds applications in optical imaging [6, 7, 8, 9, 10].

The degree of coherence determines the ability of light to form interference fringes. When two optical waves are superposed, the intensity of the total field can show a periodic spatial variation, i.e., an interference fringe pattern. The visibility of this pattern – the contrast – is proportional to the degree of mutual coherence of the waves. The fringes are absent in the case of two independent waves, but if the waves are derived from the same source, the fringe visibility depends on the temporal and spatial shift of the waves with respect to each other [11]. This property is used, e.g., in optical coherence tomography and ghost imaging [12].

It is worth noting that, within a short enough time interval, any two waves produce a perfect local interference fringe pattern. However, when the waves are mutually coherent, the pattern is stable and can be easily observed and measured. When the waves are mutually incoherent, including the case of quasi-monochromatic waves with different frequencies, the resulting interference pattern moves, in general both randomly and deterministically, and becomes completely washed out when averaged in time [13, 14].

Interferometry extends the limits of imaging systems by increasing their

resolution, both transverse and longitudinal [6, 7], and by allowing for imaging of transparent phase-shifting objects [15]. It can also be used in wavefront sensing [16], holography [17], homodyne and heterodyne detection [18, 19], and spectral analysis [20]. In this dissertation, both static and dynamic interference effects are considered to extend the capabilities of optical imaging systems and to create and measure multifrequency beating optical beams with controlled group velocity in free space.

1.1 Coherent and incoherent imaging systems using interferometry

While the longitudinal coherence used, e.g., in optical coherence tomography [7] is determined by the light bandwidth, the transverse coherence is determined by the angular size of the source. For optical imaging systems, the transverse coherence of the illumination, also called the spatial coherence, plays a crucial role. Spatially coherent illumination is characterized by a fixed phase difference between its components at any two points in the object plane. This makes the imaging system with this type of illumination linear in complex amplitude, which means that the fields originating from different points in the object plane are summed to obtain the field in the image plane. In terms of the point spread function (PSF), the complex amplitude A_i of the field in the image plane of a coherent imaging system is given by [21]:

$$A_\mathrm{i}(x,y) = h(x,y) * A_\mathrm{g}(x,y), \tag{1.1}$$

where A_g is the complex amplitude of the object field in the absence of diffraction (ideal geometric-optics image), h is the PSF of the system, and the asterisk stands for the convolution operation.

In case of incoherent illumination, the fields at different points in the object plane, and consequently also their PSFs in the image plane, do not correlate. Hence, the intensities of the PSFs, rather than the PSFs themselves, must be summed to obtain the intensity in the image plane, which is why the incoherent imaging systems are linear in intensity. The intensity distribution $I_\mathrm{i}(x,y)$ in the image plane can then be written as

$$I_\mathrm{i}(x,y) = |h(x,y)|^2 * I_\mathrm{g}(x,y), \tag{1.2}$$

where I_g is the intensity of the ideal diffraction-free image of the object and $|h(x,y)|^2$ can be called the intensity PSF of the system [21].

The width of PSF defines the two-point resolution of the imaging system. If the imaging system is diffraction-limited, i.e., there are no aberrations, its transverse resolution is determined by the Rayleigh resolution criterion. For a coherent imaging system, the resolution is equal to $0.82\lambda_0/NA$, where λ_0 is the wavelength of light in vacuum and NA is the numerical aperture of the imaging system [22]. When incoherent illumination is used, the

resolution is slightly better, given by $0.61\lambda_0/NA$, in particular because $|h(x,y)|^2$ is narrower than $|h(x,y)|$ [22].

The coherent and incoherent imaging systems differ not only by the resolution. For example, incoherent light is usually broadband and its longitudinal coherence length is small [23]. This allows one to obtain a high longitudinal resolution for three-dimensional (3D) imaging, using optical interferometry [24]. Coherent light, on the other hand, has a large longitudinal coherence length, which allows one to apply interferometric methods for significant reduction of even large optical aberrations [25]. The interferometric coherent and incoherent imaging systems are considered in general terms in the next subsections.

1.1.1 Field interferometry

In general, in an interferometric imaging system, the field originating from the object is superimposed with a reference field, and the resulting interference pattern is recorded and processed to retrieve the object's image. An example of such an imaging system is shown in Fig. 1.1. The system is based on a Mach-Zehnder interferometer consisting of a sample (upper) and a reference (lower) arm. The key advantage of this system is that, in addition to the amplitude distribution within the object, it also provides information on the phase distribution. Hence, fully transparent phase objects can be observed as well [26]. The optical path-length difference between the arms of the interferometer must be smaller than the longitudinal coherence length of the light. It is therefore preferable to use narrowband illumination. However, broadband light can also be used.

Because an incoherent light source has a small longitudinal coherence length, the interference is observed only in a narrow longitudinal range

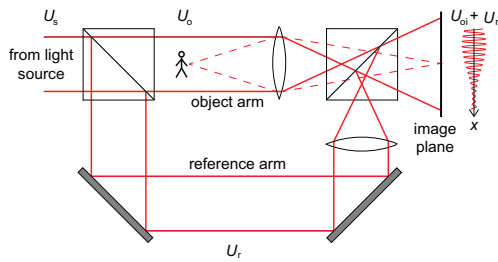

Figure 1.1. A schematic of an interferometric imaging system: an optical beam from the light source is split by a beam splitter into the object and reference arms. The object is imaged with a lens, and a similar lens is inserted in the reference arm. The beams from the two arms are combined by another beam splitter and the resulting interference pattern is recorded.

around the zero path-length difference between the interferometer's arms. This effect is used in Optical Coherence Tomography (OCT) [27]. If, on the other hand, the field has a short transverse coherence length, the interference is observed only if the arm fields are perfectly overlapping and there are no significant (greater than the coherence length) distortions produced in the imaging system [28].

If the field of the light source in front of the object is U_s, then the field distribution behind the object is $U_\mathrm{o} = TU_\mathrm{s}$, where T is the transmission function of the object. In the image plane, the corresponding field can be written as $U_\mathrm{oi} = h(x,y) * [T_\mathrm{g}U_\mathrm{g}]$, where $h(x,y)$ is the PSF of the system and T_g and U_g are the geometric-optic images of T and U_s. The reference-arm field in the image plane is given by $U_\mathrm{ri} = h(x,y) * U_\mathrm{g}\exp(i\phi)$, where ϕ is the phase difference between the arms. When the reference and sample fields are superimposed, the time-averaged intensity of the resulting field in the image plane is

$$I_\mathrm{i}(x,y) = \langle |U_\mathrm{oi}(x,y)|^2 \rangle + \langle |U_\mathrm{ri}(x,y)|^2 \rangle + 2\mathrm{Re}\{\langle U_\mathrm{oi}(x,y)U_\mathrm{ri}^*(x,y)\rangle\}, \tag{1.3}$$

where the first term is the intensity image of the object, the second term is a featureless background intensity associated with the reference arm, and the third term describes the interference of the two beams. The interference pattern depends on the object's phase distribution and the phase difference ϕ. By varying ϕ, the third term can be made to oscillate, which can be used to separate the interferometric information from the static intensity profile, as we have shown in Publication I.

Imaging systems based on optical field interferometry, such as holographic microscopes, interferometric scanners, and OCT systems, are widely used in 2D and 3D imaging, e.g., for biology [29, 30, 31], medicine [32, 33], metrology [34, 35], and optical ranging [36]. In Publication I and Publication II, field-interferometric microscopes are demonstrated to exhibit remarkable insensitivity to severe optical aberrations.

1.1.2 Intensity interferometry

When a coherent light source is used in an interferometric imaging system shown in Fig. 1.1, the interference is formed everywhere in the output beam, because any optical path difference between the arms is smaller than the longitudinal coherence length of the light. If the source is a narrowband laser, the coherence length can reach kilometers. This allows using interferometry even if the path-length difference appears to be large, for example, in the case of strong optical aberrations. This feature is widely used in optical ghost imaging systems [37]. The spatial coherence of a temporally highly coherent light in these systems is lowered by transmitting the light through a rotating ground glass plate [25, 37]. A short transverse coherence length then allows for the system to provide a high resolution of

the images, retrieved from the point-wise intensity correlations between the arms in the image plane. Thus, the system is based on intensity rather than field interferometry. When the intensity fluctuations of light are slow, the intensity correlations can be measured with two detectors by measuring the correlations of the produced electric currents. For this, the characteristic time of the intensity variations must be long compared to the response time of the detectors (on the order of 1 fs for fastest detectors [38]).

In a typical ghost imaging system, a bucket detector is placed in the sample arm to record the signal received from the object with no spatial resolution, while the reference-arm detector is assured to acquire the coordinate information, e.g. by using a scanned pinhole. A two-dimensional detector array can be used as well. The obtained distribution of the intensity correlation shows an image of the object [39].

If instead of a highly coherent light source together with a rotating ground glass plate one utilizes a spatially incoherent thermal or luminescent light source, the intensity fluctuations become too rapid to be detected by available photodetectors. In such cases, a two-photon-absorption detector can be used to measure the correlations, because the electric current produced by such a detector is proportional to the squared intensity. Hence, if at the position of the detector in the transverse plane the object and reference arms overlap, the measured signal is

$$S \propto \langle I^2 \rangle = \langle I_\mathrm{o}^2 \rangle + \langle I_\mathrm{r}^2 \rangle + 4\langle I_\mathrm{o} I_\mathrm{r} \rangle, \tag{1.4}$$

where I_o and I_r are the object and reference arm intensities, respectively, and the angle brackets denote time averaging [40]. The polarizations of the object and reference fields are assumed to be the same, and ultrafast fluctuations associated with the field interference are removed by averaging. The third term is the intensity correlation function to be measured.

Intensity interferometers can find applications in many areas of science and technology, such as imaging objects in turbulent media by means of ghost imaging [25, 37, 39], measuring the angular size of stars with astronomical interferometers [41, 42], and studying various quantum-optical phenomena [43, 44]. In addition, it can be used to study ultrafast optical phenomena, such as polarization fluctuations in broadband unpolarized light [45].

1.2 Wave beating

Beating of two interfering sound waves of slightly different frequencies is a widely known phenomenon. The volume of the beating waves varies periodically in time as the waves interfere constructively and destructively. Similarly, two optical waves with different frequencies can be superimposed

to show a sinusoidally oscillating intensity. The oscillation frequency of the field will be equal to the frequency difference of its components [11]. This can be used to obtain ultrafast intensity variations with a maximum modulation depth, which can help to improve the sensitivity and resolution of intensity interferometry [14].

Considering the simplest case of interference of two equally polarized monochromatic plane waves, we can write the total field at some point in space in the form

$$U(t) = U_1 \exp(i\omega_1 t) + U_2 \exp(i\omega_2 t), \tag{1.5}$$

where ω_1 and ω_2 are the angular frequencies of the components, and U_1 and U_2 are their amplitudes [11]. The phases are taken to be equal to zero and $t = 0$. The intensity of the total wave in this case can be written as

$$I(t) = I_1 + I_2 + 2\sqrt{I_1 I_2}\cos[(\omega_2 - \omega_1)t], \tag{1.6}$$

from which it can be seen that the intensity oscillates at a frequency equal to the frequency difference of the components. The beating period is $T_\mathrm{b} = 2\pi/|\omega_1 - \omega_2|$. For a large difference between the frequencies, the period can be very short and difficult to measure directly. However, by means of intensity interferometry based on two-photon absorption, one can relatively easily measure even femtosecond-range beating periods [40]. Beating waves can also be studied using field interferometry, as we demonstrate in Publication IV.

The wave beating phenomenon is widely used in heterodyne-type detection [46, 47]. It can also be applied in optical frequency stabilization [48, 49] and in laser mode locking [50, 51].

1.2.1 Multiple frequency beams and their group velocity

The electric field of an optical plane wave (pw) of a finite bandwidth that propagates in the z direction can be written as

$$E_\mathrm{pw}(z,t) = \int_{-\infty}^{\infty} U(k)\exp(i(kz - \omega t))dk, \tag{1.7}$$

where $U(k)$ is the amplitude of a monochromatic component of the field with the wavenumber k and angular frequency ω that depends on k (in general, nonlinearly). Using the Taylor series expansion about the central wavenumber k_0 (corresponding to the central frequency ω_0), one can write

$$\omega(k) = \omega_0 + (k - k_0)\left.\frac{d\omega}{dk}\right|_{k=k_0} + ..., \tag{1.8}$$

where the higher-order, nonlinear terms can be neglected. By doing so, we can rewrite Eq. (1.7) in the form

$$E_\mathrm{pw}(z,t) = \exp(i(k_0 z - \omega_0 t)) \int_{-\infty}^{\infty} U(k)\exp(i(k - k_0)(z - v_\mathrm{g} t))dk. \tag{1.9}$$

The envelope of this function moves along z with the speed $v_g = d\omega/dk$ that is the group velocity of the wave [11]. In free space, the group velocity is equal to the phase velocity $v_p = \omega/k$, and both are equal to the speed of light in vacuum, c. In a dispersive medium (exhibiting $k(\omega) = k_0 n(\omega)$, where n is the refractive index of the medium), the group velocity can differ from, but not exceed the speed of light in vacuum [52].

For an optical beam, containing many plane-wave components, the expansion of the electric field into monochromatic plane waves takes the form of a three-dimensional Fourier integral

$$E_b(x,y,z,t) = \iiint_{-\infty}^{\infty} U(\mathbf{k}) \exp(i(k_x x + k_y y + k_z z - \omega t)) dk_x dk_y dk_z, \qquad (1.10)$$

where k_x and k_y play the role of spatial frequencies in each given transverse plane, $k_z = k\cos\alpha$ is the projection of the wavevector $\mathbf{k}$ onto the beam axis z, and α is the plane-wave propagation angle with respect to axis z [11]. The expansion is written for polarized light in the paraxial approximation, allowing us to neglect the vector nature of the field. The on-axis field distribution (at $x = y = 0$) can be written as

$$E_b(z,t) = \int_{-\infty}^{\infty} U'(\mathbf{k}) \exp i(k_z z - \omega t) dk_z, \qquad (1.11)$$

where $U'(\mathbf{k}) = \iint_{-\infty}^{\infty} U(\mathbf{k}) dk_x dk_y$. Equation (1.11) is similar to Eq. (1.7), but it contains k_z in the place of k. Hence, the group velocity of the beam must be $v_g = d\omega/dk_z$. Since k_z depends on α, v_g depends on α and $d\alpha/d\omega$ [53]. The latter quantity is called the angular dispersion. For it not to be equal to zero, different frequency components of light must show different propagation angles. As an example, normal angular dispersion can be obtained by transmitting light through a refractive prism, and an anomalous dispersion by using a diffraction grating [11]. The possibility to control the group velocity of light by designing its angular spectrum can be used in ultrafast and nonlinear optics dealing with short laser pulses [53]. For example, the effect of angular dispersion can compensate for the group velocity dispersion in a non-linear medium, making optical pulses at different central frequencies propagate with the same speed, or provide a controlled delay for optical pulses in free space [54]. The control over the group velocity has also been demonstrated by modifying the properties of the propagation medium, such as its dispersion and absorption or gain [55, 56], and by spatially or spatio-temporally structuring the beam profile [57, 58, 59]. Various transversely accelerating Airy, Mathieu, and Weber beams [60, 61], as well as longitudinally accelerating Bessel beams [62] have been studied, and superluminal [63, 64, 65], subluminal [66, 67, 68], and even negative group velocities [69] have been achieved for these beams in free space. However, in the case of a longitudinal acceleration, the achieved group velocity obtained for a femtosecond-pulsed laser beam was seen to stay close to the speed of light in vacuum [70, 71].

Zero-order Bessel beams are probably the simplest beams in view of their angular spectrum. They are self-healing, non-diffracting optical beams composed of plane waves that propagate at a common polar angle with respect to the beam axis [72]. Therefore, they can be used as a basis for creating a multi-frequency beam with controllable group velocity. The simplest example is a two-frequency-component Bessel beam that exhibits the wave beating phenomenon. By controlling the propagation angles of the beam's plane-wave components, an arbitrary positive or negative value of the group velocity, as well as longitudinal acceleration or deceleration of the beam intensity peaks can be achieved, as we demonstrate in Publication IV.

In the case of a three-component Bessel beam, the group velocity can depend on the longitudinal coordinate and time. More than three components in a beam result in a more complicated behavior of the group velocity, and if the components have finite spectra and do not correlate, the group velocity can change both deterministically and randomly. When this happens, the amplitudes and phases of the interfering waves fluctuate, resulting in a fluctuating group velocity. In Publication III, various examples of multicomponent beams, their properties, and methods to control their group velocity have been considered in detail.

2. Interferometric imaging

2.1 Aberrations

Optical aberrations are unwanted distortions of the wavefronts of light in optical imaging systems. They can be caused by turbulent media, refractive index variation within a sample, as well as imperfect shape and misalignment of the optical components. The aberrations deform and enlarge the PSF of the imaging system, which leads to a lower resolution, distortion, and blur of the image. There are two main types of aberrations: chromatic aberrations that are caused by material dispersion of the optical components and monochromatic aberrations that include tilt, defocus, spherical aberration, coma, astigmatism, image distortion, and others [73].

It is impossible to completely eliminate all the aberrations in the imaging system, but they can be minimized. In the absence of aberrations, the imaging system is called diffraction-limited, because the resolution is limited only by diffraction. For an imaging system with a circular pupil, the resolution limit is given by the size of the Airy disk resulting from light diffraction at the pupil [74]. In Publication I and Publication II, we concentrated on reducing the aberration effects caused by the sample, the imperfections in the imaging system, and the propagation medium, but the developed methods can also be applied to compensate for other types of monochromatic aberrations.

There are several well-known imaging techniques that are able to decrease the effect of optical aberrations. One of them is called adaptive optics. The main idea is to compensate for the wavefront distortions caused by the aberrations with the help of a deformable mirror or another type of a spatial light modulator. The aberrations, however, must be measured prior their compensation. This method is widely used for imaging through turbulent optical media [75, 76, 77]. However, due to the required preliminary measurements, the technique might not be efficient in the case of aberrations that rapidly change in time, as well as strong and complex

non-deterministic aberrations. Other imaging techniques, like ghost imaging and OCT, are able to overcome any aberration without preliminary measurements, if the longitudinal shifts of the wavefront it causes are smaller than the longitudinal coherent length of the light [78, 79]. These two imaging techniques are considered in the next subsection in more detail.

2.2 Concepts of ghost imaging and OCT

Optical ghost imaging is a technique that retrieves the object image from intensity correlation or photon coincidence detection in the object and reference arms of the imaging system [80]. A general scheme of the ghost imaging setup is shown in Fig. 2.1. The system uses a spatially incoherent light beam, e.g., obtained by transmitting a coherent laser beam through a rotating ground glass. The beam is split into an object and reference arm by a beam splitter. Then, in the object arm, light is transmitted by the object and detected by a bucket detector with no spatial resolution. At the output of the reference arm, the field is transversely scanned by using a movable pinhole detector. The intensity correlation is then plotted as a function of the coordinates of this detector, revealing the image. Interestingly, the spatial information about the shape of the object is destroyed in the object arm by the bucket detector, while the reference arm never interacts with the object. Still, the image is retrieved. Hence the name "ghost imaging". Initially, the method, being based on the photon coincidence detection, was considered to have a purely quantum nature, but later it has been shown that the same results can be obtained by measuring the classical intensity correlations [81, 82]. Both quantum and classical approaches have shown the ability to significantly reduce the effect of aberrations that

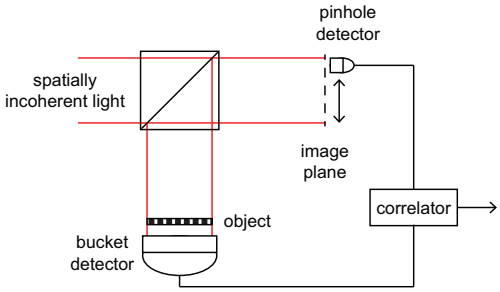

Figure 2.1. A schematic of a ghost imaging system. A spatially incoherent optical beam is split by a beam splitter into the object and reference arms. In the object arm, the beam is transmitted by the object and is detected by a bucket detector. The output of the reference arm is transversely scanned by a pinhole detector. The correlator measures the correlation of the intensity signals arriving from the two arms and retrieves the image.

can appear between the object and the bucket detector [25, 79, 83]. In fact, the image can be retrieved as long as the shifts of the wavefronts caused by the aberrations do not exceed the longitudinal coherence length of the light used in the system.

Ghost imaging systems find applications in the fields of optical microscopy, long-distance imaging through turbulent atmosphere, and remote sensing [25, 84, 85]. However, conventional ghost-imaging setups are complex and slow, because they require time for scanning the detector in the reference arm and averaging over multiple measurements. In addition, the "ghost" images often have a relatively low resolution determined by the speckle size of the illuminating light [86].

Optical Coherence Tomography is another imaging technique that is widely used in biology and medicine for non-invasive scanning of 3D objects [87]. Figure 2.2(a) shows a schematic of a typical OCT setup. The system is based on a "white-light" Michelson interferometer and uses a broadband light beam with a small longitudinal coherence length that determines the longitudinal resolution of the system. The transverse resolution is given by the beam diameter. The object is transversely scanned, producing an interference signal from a certain well-defined depth of the object. A 2D image of the object at that depth is formed by the amplitude of the interferometric intensity modulation due to a small periodic motion of the mirror in the reference arm. Then the object is shifted longitudinally, by a distance comparable with or larger than the longitudinal coherence length of the beam, to repeat the 2D scanning. In this way, a 3D image of the object is obtained. One of the variations of OCT is the Full-Field Optical Coherence Tomography (FFOCT) that does not require transverse scanning of the sample arm. Instead, it uses an expanded spatially incoherent optical beam to illuminate the sample, as shown in Fig. 2.2(b). The whole

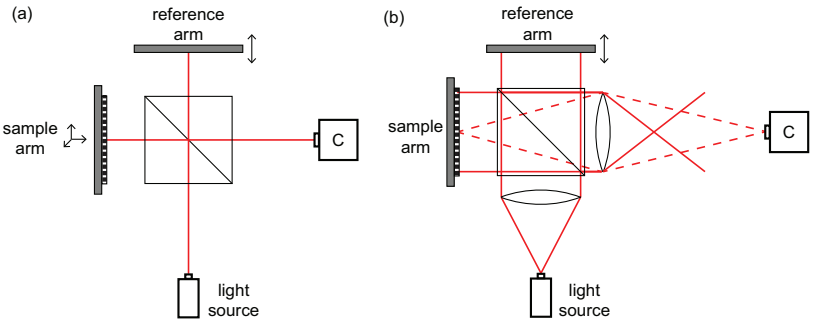

Figure 2.2. A schematic of an imaging system used for (a) OCT and (b) FFOCT. An optical beam from a broadband light source is split by a beam splitter into the sample and reference arms. After being reflected by the mirror in the reference arm and the object in the sample arm, the beams are combined again, and the resulting interference pattern is recorded by camera C. In (a), the beam is narrow and the sample is transversely scanned, while in (b) the beam is wide, producing a full-field transverse image at once.

transverse plane of the object at each given depth is imaged at once [88]. The imaging is still based on the field correlations. Light sources used in FFOCT systems are usually thermal or pseudothermal sources. Even though the longitudinal coherence length obtained with such light sources is considerably shorter than that used in ghost imaging systems, both OCT and FFOCT are able to reduce the influence of small aberrations on the image [78, 87].

Similarly to FFOCT systems, the interferometric imaging systems described in Publication I and Publication II are based on the measurement of the optical field correlation. However, similarly to the ghost imaging systems, they use light with a large longitudinal coherence length. These new systems can therefore exhibit a high transverse resolution even in the presence of severe aberrations that would normally destroy the image completely. The approach is described in detail in the next section.

2.3 Aberration-insensitive interferometric imaging

We have introduced an optical microscope based on a Mach-Zehnder interferometer for imaging light-transmitting objects in the presence of strong aberrations. The setup is shown in Fig. 2.3. It uses a highly spatially incoherent light-emitting diode (LED) as a light source of central wavelength $\lambda_0 = 632$ nm and bandwidth $\Delta\lambda = 18$ nm. The light is collimated by a microscope objective and transmitted through a linear polarizer oriented at 45° with respect to the vertical direction to make the vertical and horizontal components of the electric field mutually correlated. The polarizing beam splitter then splits the light into the object and reference arms. A pair of

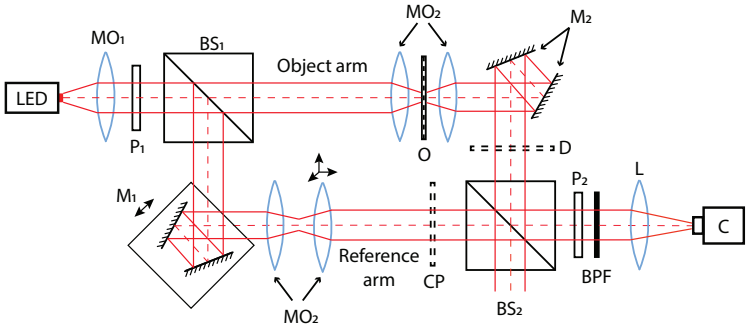

Figure 2.3. Interferometric imaging system for light-transmitting objects: MO_1 and MO_2 – 10× and 5× microscope objectives, respectively; P_1 and P_2 – linear polarizers; BS_1 and BS_2 – beam splitters; M_1 and M_2 – mirrors; O – object; D – diffuser; CP – compensating glass; BPF – bandpass filter; L – lens; C - camera. In the reference arm, the pair of mirrors M_1 can be translated along the direction shown by the arrows, and one of the microscope objectives can be moved in three directions. The figure is reproduced from Publication I with the permission of AIP Publishing.

microscope objectives is placed into both interferometer arms at an equal light-propagation distance from the first beam splitter. In the object arm, the first objective projects the LED image onto the sample surface, and the second objective collimates the light transmitted through the sample. In the reference arm, the objectives are used to transversely flip the beam, as in the object arm, and to fine-tune the wavefront curvature and the transverse position of the beam by moving the second microscope objective, as indicated by arrows in Fig. 2.3. We used two tilted mirrors at the corners of each arm to turn the beam towards the second beam splitter and to modulate the path-length difference between the arms without moving the beams. For that reason, when the optical path length of the reference arm is changed by moving the mirror pair (along the arrows shown in Fig. 2.3), the position of the beam propagating towards the second beam splitter stays the same. The object and the reference beams are combined by the second beam splitter and transmitted through a linear polarizer with tilted transmission axis to make the two orthogonally polarized beams interfere. The resulting interference pattern is focused onto the camera sensor with a lens. The longitudinal coherence length of the light source is increased from $L_c = \lambda_0^2/\Delta\lambda = 22$ μm to about 0.4 mm by inserting a bandpass filter (BPF) of 1-nm bandwidth into the system. Without aberrations, the resolution of the system is $0.6\lambda_0/NA \approx 3$ μm, where $NA = 0.12$ is the numerical aperture of the microscope objective behind the object. Note that the method is applicable also to systems with high NA objectives. To test the system, we either introduced a deterministic focusing error by shifting the camera away from the focal plane, or placed a random diffuser into the object arm that completely destroys the image. A compensating glass plate of the same thickness as the diffuser is placed into the reference arm to maintain the optical path lengths in the arms equal.

The interferometric image of the object is acquired by slightly altering the length of the reference arm and recording a short video of the moving interference pattern. As we use an incoherent light source with extended emitting area, each point of it only produces interference with itself, and the size of interfering spots in the beams is equal to their transverse coherence length. Using a simple example of a pinhole as an amplitude object to be imaged, the interferometric image formation in the presence of aberrations can be explained as follows. Being enlarged and deformed by aberrations, the PSF of the object arm meets with the diffraction-limited PSF of the corresponding point in the reference arm, and the interference appears only in the overlapping area, whose size is defined by the second PSF. The computer processing of the video data includes finding the difference between the maximum and minimum intensity values at each pixel, which cleans the interferometric signal from the static background. The processed signal retrieves the image, because light removed by the object does not interfere with the reference arm and does

not contribute to this signal. Thus, a sharp image with approximately diffraction-limited resolution is obtained. The schematic of the process is illustrated in Fig. 2.4(a)-(c).

In the case of imaging a transparent phase-shifting object in the presence of aberrations, the procedure is the same. The reference arm length is altered and a short video of moving interference fringes is recorded for further processing. The procedure is shown in Fig. 2.4(d)-(f). Consider a transparent flat sample consisting of two areas of different thickness that cause different phase shifts. The interference pattern formed by the object and reference beams covers the whole area of the sample, but at the border between the two areas the fringe contrast is low due to spatial averaging provided by diffraction. The width of the observed border line in the final image is determined by the size of the diffraction-limited PSF of the reference arm. Thus, the retrieved image contains relatively narrow contours of changing thickness of the object. The value of the phase shift between the areas can be evaluated from the shift of the interference fringes at the border.

The resolution and the intensity distribution of the interferometric image can be calculated within the paraxial approximation using scalar wave optics. As discussed also in the Introduction, the fields from the reference and sample arms of the system can be written as follows

$$U_{\mathrm{r}}(u,v) = h(u,v) * U_{\mathrm{go}}(u,v)\exp(i\phi_{\mathrm{rs}}), \tag{2.1}$$

$$U_{\mathrm{s}}(u,v) = h_{\mathrm{ab}}(u,v) * [T_{\mathrm{g}}(u,v)U_{\mathrm{go}}(u,v)], \tag{2.2}$$

where u and v are the transverse coordinates in the image plane, $h(u,v)$ is the PSF of the imaging system in the absence of aberrations, $U_{\mathrm{go}}(u,v)$ and $U_{\mathrm{go}}(u,v)\exp(i\phi_{\mathrm{rs}})$ are the geometric-optics images of the field incident

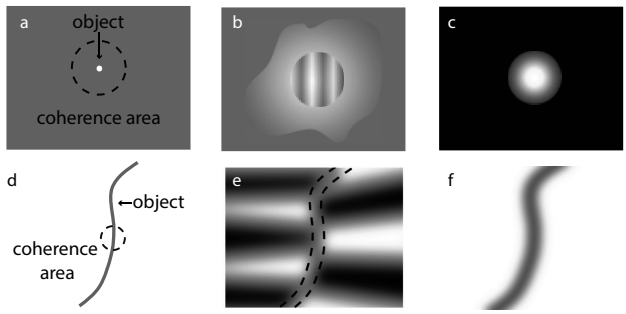

Figure 2.4. Schematic of the formation of the interferometric image of an amplitude (a)-(c) and a phase (d)-(f) object in the presence of aberrations. The pictures from left to right in each row show: (a) and (d) show the object to be imaged and the coherence area of the system within the circular dashed line, (b) and (e) show the interference patterns produced by light of the aberrated sample arm and the diffraction-limited reference arm, and (c) and (f) illustrate the retrieved ghost image. The figure is reproduced from Publication I with the permission of AIP Publishing.

on the sample in the object arm and on the corresponding plane between the objectives in the reference arm, respectively, ϕ_{rs} is the tunable path-length phase difference between the arms, $h_{ab}(u,v)$ is the PSF affected by aberrations, $T_g(u,v)$ is the geometric-optics image of the complex amplitude transmission function of the object. Then, the time-averaged intensity of the total field in the image plane can be written as

$$I(u,v) = \langle |U_s(u,v)|^2 \rangle + \langle |U_r(u,v)|^2 \rangle + 2\mathrm{Re}\{\langle U_s(u,v) U_r^*(u,v) \rangle\}, \tag{2.3}$$

where the angle brackets denote time averaging. When the phase difference ϕ_{rs} changes, the intensity at each coordinate (u, v) changes as well. The intensity profile of the retrieved image is calculated by subtracting the minimum value of $I(u,v)$ from its maximum value at each (u,v). The phase difference ϕ_{rs} must change at least by 2π. As we have shown in Publication I, the retrieved image intensity is

$$\begin{aligned} I_{retr}(u,v) &= 4\mathrm{Re}\{\langle U_s(u,v) U_r^*(u,v) \rangle\} = \\ &= 4I_{go} \times \mathrm{Re}\Big\{ \int_{-\infty}^{\infty} \int_{-\infty}^{\infty} h_{ab}(u-x, v-y) h^*(u-x, v-y) \\ &\times |T_g(x,y)| \exp(i[\phi_T(x,y) - \phi_{rs}]) dx dy \Big\} \Big|_{max}, \end{aligned} \tag{2.4}$$

where "max" refers to the maximum value of the function. The phase $\phi_T(x,y)$ is related to the transmission function of the object $T_g(x,y)$. After simplifying Eq. (2.4), we obtain for an amplitude object in the absence of aberrations ($h_{ab} = h$) the following intensity distribution

$$I_{retr}(u,v) \propto |h(u,v)|^2 * |T_g(u,v)|. \tag{2.5}$$

When strong aberrations are introduced into the object arm, the aberrated PSF $h_{ab}(u,v)$ becomes wide compared to $h(u,v)$, and Eq. (2.5) can be approximated as

$$I_{retr}(u,v) \propto |h(u,v)| * |T_g(u,v)|. \tag{2.6}$$

If the object is a pinhole, whose transmittance function can be written as $T_g(u,v) = \delta(x,y)$, its retrieved image becomes given by the PSF of the system, $I_{retr,\ pinhole}(u,v) \propto |h(u,v)|$, as we have shown in Fig. 2.4(c).

Similarly, for a phase object with two different phase-shifting areas separated by a straight line along the v-axis, the transmission function can be written as $T_g(u,v) = 1 - 2H(u)$, where $H(u)$ is the Heaviside step function. Here the phase shifts differ by π. In the absence of aberrations, the retrieved intensity distribution is

$$I_{retr}(u,v) \propto ||h(u,v)|^2 * [1 - 2H(u)]|. \tag{2.7}$$

The intensity smoothly decreases towards zero when u is approaching zero, resulting in a dark line parallel to the v-axis. The width of the line is

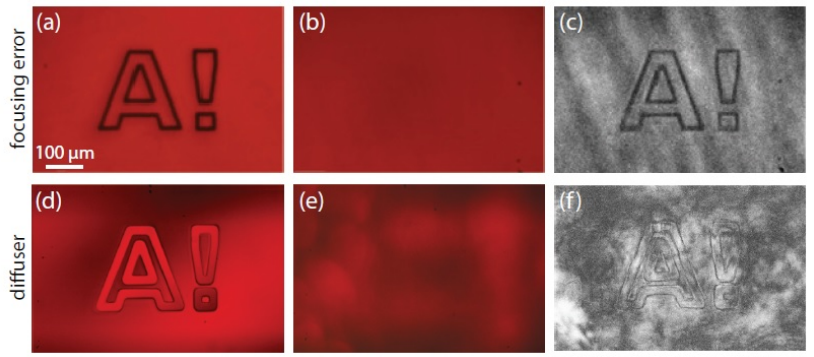

Figure 2.5. Optical images of (a) an amplitude-modulated and (d) a phase-modulated logo of Aalto University obtained using the setup shown in Fig. 2.3. In each row, the leftmost and the middle images are, respectively, obtained without and with a focusing error [cases (a) and (b)] or an optical diffuser [cases (d) and (e)]. Image (a) is taken from the reference arm alone, while image (d) was obtained with both interferometer arms open. The rightmost images are the retrieved interferometric images. The figure is reproduced from Publication I with the permission of AIP Publishing.

determined by the width of $|h(u,v)|^2$. As before, in the presence of strong aberrations in the object arm, the aberrated PSF is wide, and therefore, the width of the dark line slightly increases, as can be seen from

$$I_{\mathrm{retr}}(u,v) \propto ||h(u,v)| * [1-2H(u)]|. \tag{2.8}$$

Some of our experimental results are shown in Fig. 2.5. In (a), a sharp intensity image of the amplitude-modulated logo of Aalto University is presented. The logo is composed of 8 μm thick metal stripes on a glass substrate. In (b), a deterministic focusing error is demonstrated. The image is seen to disappear. When the reference arm is opened, an image of the object appears in the moving interference pattern. Calculating the distribution of the modulation amplitude from the recorded video gives the final image, case (c). In the image, also a sharpened pattern of the emitting surface of the LED source can be seen. The images in (d)-(f) demonstrate the performance of the setup when imaging phase-modulated objects. The object has been fabricated by etching the logo pattern in a photoresist film on a glass substrate. The lines in the logo are 24 μm wide. With both arms opened, we obtain a sharp image of the logo as shown in (d). After screening the logo with a diffuser, we cannot reveal any details of the object as can be seen in (e). However, by modulating the phase difference between the arms and processing the interferometric signal, we retrieve the image shown in (f). The contours of the phase object clearly appear on the background of random intensity variations caused by the diffuser.

The proposed imaging method can also be applied to reflecting and back-scattering objects. For that, we have designed a different imaging system

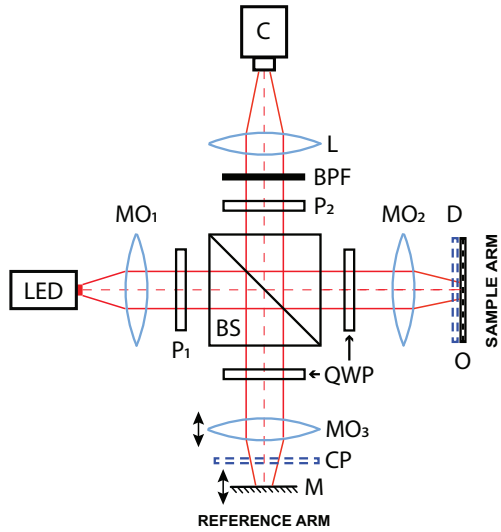

Figure 2.6. Interferometric imaging system designed for reflecting and back-scattering objects: MO_1, MO_2, and MO_3 – 10×, 4×, and 4× microscope objectives, respectively; P_1 and P_2 – linear polarizers; BS – polarizing beam splitter; QWP - quarter-wave plate; M – mirror; O – object; D – diffuser; CP – compensating glass plate; BPF – bandpass filter; L – lens; C - camera. In the reference arm, mirror M and microscope objective MO_3 can be translated along the direction shown by the arrows. The figure is adapted with permission from Publication II © Optica Publishing Group.

based on a Michelson interferometer. The setup is shown in Fig. 2.6. The working principle is similar to that of the setup based on a Mach-Zehnder interferometer: an LED is used to produce spatially incoherent light that is collimated by a microscope objective and transmitted through a linear polarizer oriented at 45° with respect to the vertical direction. A polarizing beam splitter divides the beam into the reference and sample arms. In both arms, a quarter-wave plate turns the polarization plane of the beam by 90° in total, so that light reflected from the mirror or the sample surface can propagate through the beam splitter towards the camera. The microscope objectives project the image of the emitting surface of the LED onto the object and mirror planes in the two arms. In the reference arm, the microscope objective and the mirror can be moved along the optical axis to tune the optical path difference between the arms. The beams coming from the sample and reference arms are combined by the beam splitter, transmitted through another linear polarizer with tilted transmission axis, and focused onto the camera detector with a lens. A band-pass filter is used to increase the longitudinal coherence length of the system to about 0.4 mm. The resolution of the imaging system in the absence of aberrations in the sample arm can be calculated as $0.6\lambda_0/NA = 3.8$ μm, where $NA = 0.10$ is the numerical aperture of the microscope objective in front of the sample.

The system was tested by using the same objects as in the previous setup.

After introducing an aberration into the sample arm and compensating for the length difference of the reference arm, the interferometric image was obtained (by changing the reference arm length and recording the moving interference pattern). By calculating the difference between the maximum and minimum values of the intensity of each pixel, the static background intensity was removed and a sharp image of the object was obtained. As we have shown in Publication II, the intensity distribution in this image is

$$I_{\mathrm{int}}(u,v) \propto |h_{\mathrm{im}}(u,v) g(u,v) * R(u,v)|, \tag{2.9}$$

where u and v are the transverse coordinates, $h_{\mathrm{im}}(u,v)$ is the PSF of light propagating from the object to the camera, $g(u,v)$ is the transverse coherence function of the aberration-free field illuminating the sample (corresponding to the field incident on the mirror in the reference arm), and $R(u,v)$ is the geometric-optics image of the object, i.e. its reflection coefficient. As the imaging system operates in the reflecting mode, the effect of each type of aberrations should be considered separately. For a severe focusing error, $h_{\mathrm{im}}(u,v)$ becomes wide compared to the diffraction-limited $g(u,v)$ and the resulting interferometric image appears sharp. However, the diffuser induces a random phase distribution in the field illuminating the object. Therefore, in Eq. (2.9) we consider the whole complex PSF including its phase (in contrast to Eq. (2.6), where the phase is neglected by considering the absolute value of PSF). Otherwise, some details of the object can be lost in the image retrieval processing. Propagation of light through the diffuser to the object can be described with a point-spread function $h_{\mathrm{obj}}(u,v)$. The width of this function is $\delta_{\mathrm{obj}} = \delta_0 + 2d\sin\theta$, where $\delta_0 = 0.6\lambda_0/NA$ is the width of the PSF without aberrations and d is the distance between the object and the diffuser. We approximate the diffuser as an array of microlenses, each with numerical aperture $\sin\theta$. Therefore, the resolution of the interferometric image obtained with a diffuser can be worse than that in the case of a focusing error. The resolution of the retrieved image is still better than that of the ordinary intensity image, whose PSF is affected by the diffuser twice. The smaller the distance between the sample and the diffuser and the smaller the diffuser grains, the higher the resolution of the retrieved image.

Similarly, a transparent phase-modulated object, e.g. with a reflection coefficient $R(u,v) = 1 - 2H(u)$ that corresponds to an object consisting of two areas of different thickness separated by a border parallel to the v-axis, can be considered. The intensity distribution in the retrieved image of this object is

$$I_{\mathrm{int}}(u,v) \propto |h_{\mathrm{im}}(u,v) h_{\mathrm{obj}}(u,v) * [1 - 2H(u)]|, \tag{2.10}$$

where $h_{\mathrm{obj}}(u,v) = g(u,v)$ in the case of a focusing error. Therefore, the width of the border line in the retrieved image is determined by the width of $g(u,v)$. If the object is screened with a random scattering layer, $h_{\mathrm{obj}}(u,v)$ becomes wide compared to $g(u,v)$ and speckled, and the image intensity

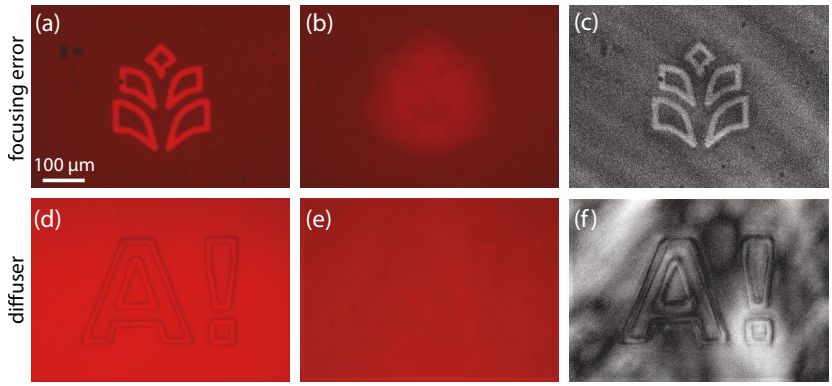

Figure 2.7. Optical images of (a) an amplitude-modulated logo of University of Eastern Finland and (d) a phase modulated logo of Aalto University obtained using the Michelson-interferometer-based setup. In each row, the leftmost and the middle images are, respectively, obtained without and with a focusing error [cases (a) and (b)] or an optical diffuser [cases (d) and (e)]. Image (a) is taken from the reference arm alone, while image (d) was obtained with both interferometer arms open. The rightmost images are the retrieved interferometric images. The figure is adapted with permission from Publication II © Optica Publishing Group.

gains random variations. However, the contours of the object described by Eq. (2.10) can be well recognized.

Examples of retrieved images can be seen in Fig. 2.7. Picture (a) shows a sharp intensity image of the amplitude-modulated logo of the University of Eastern Finland. The logo is composed of 12 µm-wide metal stripes on a glass substrate. The effect of a deterministic focusing error is demonstrated in (b), where the image of the logo is severely blurred. After opening the reference arm and recording the video of the moving interference fringes, the video processing algorithm was applied and the final image (c) was obtained. The retrieved image contains a sharp image of the logo and a sharpened pattern of the emitting surface of the LED source in the background. Pictures (d)-(f) demonstrate imaging of a transparent phase-modulated object. The object is a negative of the one shown in Fig. 2.5(d). The image shown in (d) was obtained with both interferometer arms opened. After inserting the diffuser into the sample arm, none of the details of the object could be resolved, as can be seen from picture (e). The interferometric imaging then allowed us to retrieve the image shown in (f). Even though the reflection from the transparent object is low, we were able to retrieve the contours of the phase object and sharpen the diffuser pattern.

Both setups have demonstrated remarkable insensitivity to deterministic and random aberrations and the ability to produce sharp images of light transmitting, reflecting, and back-scattering objects that can be amplitude and/or phase modulated. Besides that, the imaging system based on the Michelson interferometer can be switched to the FFOCT mode by removing

the band-pass filter and used to image three-dimensional objects. The proposed imaging method can find applications in microscopy of biological and medical samples, with the features to be observed being located behind an aberrating and scattering layer of a transparent tissue.

3. Multifrequency Bessel beams

3.1 Bessel beams with adjustable group velocity in free space

Bessel beams are diffraction-free solutions of the Hemholtz equation in cylindrical coordinates [89]. In our studies, we consider a zeroth-order Bessel beam that is formed by a plane wave transmitted through an axicon. If the plane-wave field is incident normally on the axicon, linearly polarized along the x axis, and propagating in the z-direction, then the electric field components of the resulting Bessel beam are

$$\begin{aligned} E_x &= E_0[(\cos\alpha+1)J_0(\sin\alpha k_0\rho)-(\cos\alpha-1)\cos 2\phi J_2(\sin\alpha k_0\rho)]\times \\ &\times \exp[\mathrm{i}(\cos\alpha k_0 z-\omega t)], \\ E_y &= E_0(1-\cos\alpha)\sin 2\phi J_2(\sin\alpha k_0\rho)\exp[\mathrm{i}(\cos\alpha k_0 z-\omega t)], \\ E_z &= -2\mathrm{i}E_0\sin\alpha\cos\phi J_1(\sin\alpha k_0\rho)\exp[\mathrm{i}(\cos\alpha k_0 z-\omega t)], \end{aligned} \tag{3.1}$$

where E_0 is the complex amplitude of the plane wave incident on the axicon, ω its angular frequency, and k_0 its wave number. The refracted plane-wave components of the beam propagate at an angle α with respect to the z-axis. The functions J_i are Bessel functions of the first kind of order i, ρ and ϕ are, respectively, the radial coordinate and azimuthal angle in the cylindrical system of coordinates [90].

In the case of broadband pulsed Bessel beams with correlated frequency components, one can use the material dispersion of the axicon to control the on-axis group velocity of the beam in free space. Since the refraction angle of the axicon (α) is a function of frequency ω, the transmitted pulsed beam has angular dispersion of

$$\partial_\omega\alpha=\frac{\cos\frac{\gamma}{2}\partial_\omega n}{\sqrt{1-\left(n\cos\frac{\gamma}{2}\right)^2}}, \tag{3.2}$$

where γ is the apex angle and n the refractive index of the axicon. Equation (3.2) shows that the angular dispersion of the beam, $\partial_\omega\alpha$, is pro-

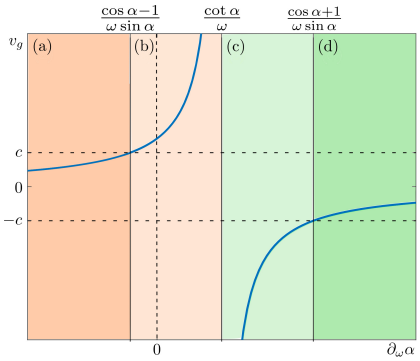

Figure 3.1. Group velocity of an angularly dispersed pulse of light as a function of angular dispersion $\partial_\omega\alpha$ (blue line). The velocity is divided into four regimes: (a) positive subluminal, (b) positive superluminal, (c) negative superluminal, and (d) negative subliminal. The figure is reproduced from Publication III with the permission of IOP Publishing.

portional to the material dispersion of the axicon $\partial_\omega n$. Other methods of creating Bessel beams with controlled angular dispersion include using holographic axicons, in which anomalous angular dispersion takes place due to the properties of diffraction [91], and utilizing a ring-shaped aperture and the Fourier-transform property of a lens, whose chromatic aberration introduces the angular dispersion into the resulting Bessel beam [92].

In general, the on-axis group velocity of a pulsed beam with an angular dispersion is given by Publication III as

$$v_g = \frac{c}{\cos\alpha - \omega\sin\alpha\partial_\omega\alpha}. \tag{3.3}$$

The dependence of the group velocity of a pulse on its angular dispersion obtained from Eq. (3.3) is shown in Fig. 3.1. It can be seen that subluminal group velocities ($v_g < c$) are achieved when the anomalous dispersion of a pulse is high, i.e., $\partial_\omega\alpha < (\cos\alpha - 1)/(\omega\sin\alpha)$. Pulses with the dispersion lying in the range of $(\cos\alpha - 1)/(\omega\sin\alpha) < \partial_\omega\alpha < \cot\alpha/\omega$ have superluminal group velocities ($v_g > c$). Finally, when the angular dispersion of a pulse is $\partial_\omega\alpha > \cot\alpha/\omega$, the group velocity is negative, which means that on the beam axis the pulse moves towards the light source.

As we have shown in Publication III, a pulse with a negative group velocity can be generated by an axicon made of zinc selenide (ZnSe). This material has a high refractive index and a high material dispersion, which results in a significant angular dispersion [see Eq. (3.2)]. Figure 3.2 demonstrates the group velocity of a pulsed Bessel beam formed by a ZnSe axicon with an apex angle of $\gamma = 136°$ as a function of the central wavelength of the pulse. For the wavelengths in the range between 550 nm and 600 nm, the on-axis group velocity of the pulse takes negative values. To illustrate this phenomenon, we have calculated a time series of

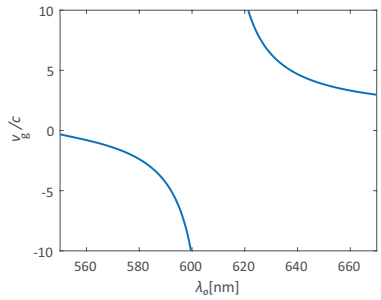

Figure 3.2. The group velocity as a function of the central wavelength of a pulse transmitted through a ZnSe axicon with an apex angle of 136°. The figure is reproduced from Publication III with the permission of IOP Publishing.

the normalized intensity distribution of a pulse with a central wavelength $\lambda_0 = 580$ nm and a full width at half maximum (FWHM) of 5 nm, using Eq. (3.1). The result can be seen in Fig. 3.3. The intensity peak of the pulse moves in the negative z-direction with group velocity $v_g = -2c$. For a more detailed explanation of the negative group velocity, we have plotted the intensity distribution of the pulse in logarithmic scale to make the low intensity regions more visible, as illustrated in Fig. 3.4. After being refracted by the axicon, the plane-wave components of the pulse propagate at an angle $\alpha = 59°$ with respect to the z-axis. Due to the angular dispersion

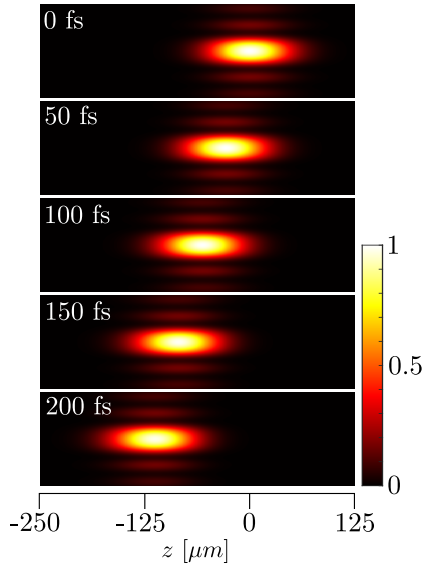

Figure 3.3. A time series of the normalized intensity distribution for a pulsed Bessel beam propagating at $v_g = -2c$. The central wavelength and FWHM of the beam spectrum are 580 nm and 5 nm, respectively. The figure is reproduced from Publication III with the permission of IOP Publishing.

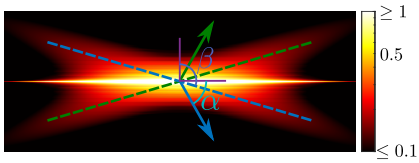

Figure 3.4. The longitudinal intensity distribution of a pulsed Bessel beam of Fig. 3.3 plotted in logarithmic scale. The pulse intensity has an X-shaped distribution with orientation along the blue and green dashed lines that are tilted by angle $\beta = 106.5°$. When the pulse propagates, these lines move along the arrows with the respective colors; $\alpha = 59°$. The figure is reproduced from Publication III with the permission of IOP Publishing.

induced by the axicon, the pulse has an X-shaped profile as shown by the dashed lines in Fig. 3.4. The tilt angle between the lines is $\beta = 106.5°$, and they move along the arrows with the respective colors. Clearly, the intersection of the refracted plane-wave components moves backwards, i.e., in the negative z-direction. The X-shaped light bullets with negative group velocity in vacuum have been demonstrated also previously [69]. However, our method of generating such pulses is much simpler.

The described pulsed Bessel beams with correlated frequency components have a deterministic intensity distribution and time evolution [1]. Continuous-wave (cw) Bessel beams consisting of several non-correlated frequency components, which we consider next, are not fully predictable. However, the intensity beating of the beam can be treated as harmonic within the so-called beating harmonicity time, i.e., the time during which the normalized intensity given by the correlation function decreases to the value of 1/2. This time is

$$\tau_{\mathrm{bh}} = 2\frac{\sum_{l=1}^{N}\overline{I_l}}{\sum_{l=1}^{N}\Delta\omega_l\overline{I_l}}, \tag{3.4}$$

where $\overline{I_l}$ is the average intensity and $\Delta\omega_l$ is the spectral width of the beam with index l. It can be seen from Eq. (3.4) that if the components have narrow spectra compared to their frequency separation, the beating harmonicity time is long compared to the beating period. This makes the intensity distribution of the beam and its evolution well predictable [14, 93].

Let us consider a beam that contains several co-propagating narrowband components. Assuming that these components are paraxial beams with the same polarization, the complex amplitude of the total field at the beam axis can be written as

$$E(z,t) = \sum_{l=1}^{N} E_l \exp[i(k_{zl}(\omega_l)z - \omega_l t + \phi_l)], \tag{3.5}$$

where E_l and ϕ_l are the amplitude and phase of the beam component with index l, respectively. The longitudinal wavenumber $k_{zl}(\omega_l)$ depends on the

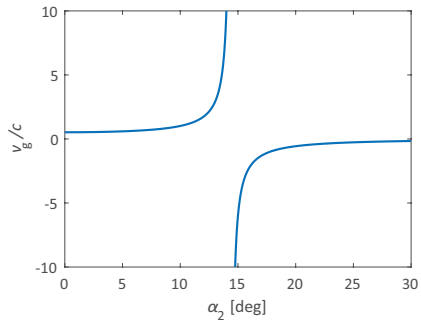

Figure 3.5. The on-axis group velocity of a two-component Bessel beam as a function of propagation angle α_2 of the second beam component. The figure is reproduced from Publication III with the permission of IOP Publishing.

angular frequency ω_l. The intensity of the total field is proportional to

$$|E(z,t)|^2 = \sum_{l=1}^{N} E_l^2 + 2\sum_{n=1}^{N-1}\sum_{m=n+1}^{N} E_n E_m \cos[(k_{zm}-k_{zn})z - (\omega_m-\omega_n)t + \phi_m - \phi_n]. \tag{3.6}$$

Equation (3.6) shows that the intensity pattern along the beam axis contains a constant term and terms describing beating pairs of the beam components. The local group velocity with which the beating intensity pattern moves along the beam axis can be found either directly by calculating the time series of Eq. (3.6), or analytically by calculating the time derivative of the coordinate of a chosen intensity peak $\zeta(t)$. To find $\zeta(t)$, the following two equations should be solved: $\partial_z |E(z,t)|^2\big|_{z=\zeta(t)} = 0$ which determines the extremum point, and $\partial_{zz} |E(z,t)|^2\big|_{z=\zeta(t)} < 0$ which defines the intensity maximum. The on-axis group velocity of a multicomponent beam can be written in terms of the obtained ζ as (see Publication III)

$$v_g = \frac{\sum_{n=1}^{N-1}\sum_{m=n+1}^{N} E_n E_m (k_{zm}-k_{zn})(\omega_m-\omega_n)\cos[(k_{zm}-k_{zn})\zeta - (\omega_m-\omega_n)t + \phi_m - \phi_n]}{\sum_{n=1}^{N-1}\sum_{m=n+1}^{N} E_n E_m (k_{zm}-k_{zn})^2\cos[(k_{zm}-k_{zn})\zeta - (\omega_m-\omega_n)t + \phi_m - \phi_n]}. \tag{3.7}$$

To illustrate the obtained results, we have considered two- and three-component Bessel beams. For a two-component beam, the group velocity is shown in Fig. 3.5 as a function of the propagation angle α of one of the components. For simplicity, the components are considered to be narrowband, and the phases ϕ_l are all set to zero. In this case, the on-axis group velocity is given by

$$v_g = \frac{(\omega_2-\omega_1)c}{\omega_2\cos\alpha_2 - \omega_1\cos\alpha_1}. \tag{3.8}$$

The wavelengths of the components are chosen to be $\lambda_1 = 610$ nm and $\lambda_2 = 600$ nm, and the fixed plane-wave propagation angle is $\alpha_1 = 10°$. It can

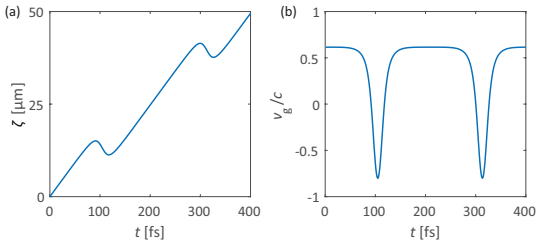

Figure 3.6. The intensity peak position (a) and the corresponding local group velocity (b) for an intensity peak of a three-component Bessel beam. The figure is reproduced from Publication III with the permission of IOP Publishing.

be seen that, by varying the propagation angle of the second component, both superluminal and subluminal group velocities, including negative ones, can be obtained. As mentioned earlier, the components of the beam are not correlated. Therefore, their phases ϕ_l must fluctuate independently, affecting the instantaneous value of the group velocity. For narrowband components, the relative phase drift is slow and the resulting change in the value of the group velocity is insignificant,

$$\Delta v_g = \frac{L_b}{2\tau_{bh}} = \frac{c\pi\Delta\omega}{2(\omega_2\cos\alpha_2 - \omega_1\cos\alpha_1)}, \tag{3.9}$$

where L_b is the beating period along the z-axis. If the beam components have the same bandwidth $\Delta\omega$ and $\Delta\omega << \omega_2 - \omega_1$, the random changes of the group velocity can be neglected.

For a three-component Bessel beam, a possible behavior of the coordinate of the peak intensity and the group velocity is demonstrated in Fig. 3.6. The following wavelengths and propagation angles have been chosen: $\lambda_1 = 610$ nm, $\alpha_1 = 10°$, $\lambda_2 = 605$ nm, $\alpha_2 = 5°$, $\lambda_3 = 600$ nm, and $\alpha_3 = 10°$. These parameters result in quite different pair group velocity values: $v_g^{12} \approx 0.42c$, $v_g^{13} \approx 1.02c$, and $v_g^{23} \approx -2.62c$. It can be seen that within a beating period, the local group velocity varies significantly, taking both negative and positive values. If the beam components are narrowband, the periodic behavior of the group velocity can be considered as deterministic.

3.2 Longitudinally accelerating Bessel beams in free space

If the propagation angle α of the plane-wave components is a function of coordinate z, the group velocity is a function of z as well, resulting in a longitudinal acceleration of the beam in free space. To obtain such an accelerating Bessel beam, one can transmit a Gaussian beam through an axicon placed in front of a lens. The lens will make the on-axis angle α

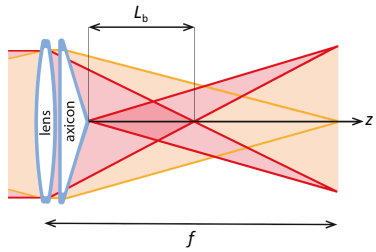

Figure 3.7. Formation of a longitudinally accelerating two-component Bessel beam. The frequency components are presented in red and orange colors. The acceleration is achieved in the intersection region of the two components within the length L_b of the beam. The figure is adapted with permission from Publication IV © Optica Publishing Group.

depend on z in accordance with (see Publication III)

$$\alpha(z) = \arctan \frac{f \tan \alpha_{||}}{f - z}, \tag{3.10}$$

where f is the focal length of the lens and $\alpha_{||}$ is the refraction angle near the center of the lens. This equation is valid for $|f - z| >> z_R$, where z_R is the Rayleigh range of the beam. The group velocity of such a beam depends on α, as can be seen from Eq. (3.8). A more significant acceleration can be achieved for a two-frequency-component beam by using a diffractive lens that, owing to strong chromatic aberrations, will make the angles α different for the components [94].

We have proposed and demonstrated a more efficient way to create a strongly accelerating two-component cw Bessel beam. The method is based on overlapping a collimated and a slightly focused beam before transmitting them through the axicon (see Fig. 3.7). As an example, let the wavelengths of these beams be $\lambda_1 = 610$ nm and $\lambda_2 = 600$ nm, respectively, and the plane-wave propagation angle of the first component fixed at

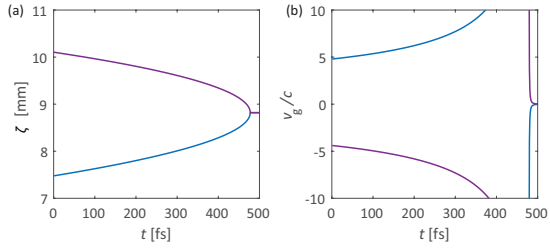

Figure 3.8. The intensity peak positions (a) and the corresponding local group velocities (b) for the two peaks with initial positions ζ of 7.5 and 10 mm of a longitudinally accelerating two-component Bessel beam. The figure is reproduced from Publication III with the permission of IOP Publishing.

$\alpha_1 = 10°$. The angle of the second component is given by

$$\alpha_2 = \arctan \frac{z_f \tan(10°)}{z_f - z}, \tag{3.11}$$

where $z_f = 5$ cm is the distance from the axicon tip to the focal plane of the focused beam. Figure 3.8(a) demonstrates the calculated positions of two moving intensity peaks with their initial positions at distances $z = 7.5$ mm and $z = 10$ mm away from the axicon tip. The peaks are seen to move towards each other with acceleration. When approaching the coordinate $z = 8.8$ mm, the group velocities of the peaks approach $-\infty$ and $+\infty$ and abruptly drop to 0, as can be seen from Fig. 3.8(b).

To demonstrate an accelerating multifrequency Bessel beam experimentally, we have designed a setup shown in Fig. 3.9. It is based on a Michelson interferometer, allowing manipulating the two frequency components of the beam independently. The wavelengths of the lasers used are $\lambda_1 = 632.8$ nm and $\lambda_2 = 657.5$ nm, and their bandwidths are $\Delta\lambda < 0.01$ pm. Since the lasers are narrowband, we can consider them as monochromatic. Therefore, the motion of the beam's intensity peaks can be assumed to be fully predictable. In the setup, the laser beams are polarized orthogonally and combined by a polarizing beam splitter. The combined beam is expanded to about 1" diameter by a microscope objective and a collimating lens. The second polarizing beam splitter separates the frequency components sending them into the two arms of the interferometer. Each arm contains

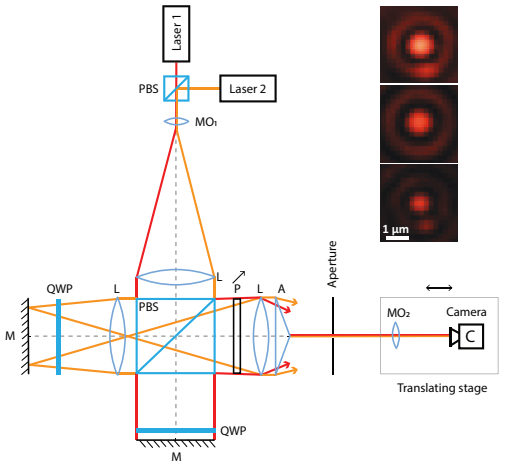

Figure 3.9. Experimental setup for generating an accelerating Bessel beam: PBS – polarizing beam splitter; MO_1 and MO_2 – 40× and 20× microscope objectives, respectively; L - lens; QWP – quarter-wave plate; M – mirror; P – linear polarizer; A – axicon. At the output, MO_2 and camera can be translated along the direction shown by the arrows. The wavelength of Laser 1 is 632.8 nm and that of Laser 2 is 657.5 nm. The inset shows the profiles of the beam as a whole (top) and its components produced by Laser 1 (middle) and Laser 2 (bottom). The figure is adapted with permission from Publication IV © Optica Publishing Group.

a quarter-wave plate for rotating the polarization plane of the beam by 90° in total, so that the beam can propagate towards the camera after being reflected from the mirror. In one of the arms, a lens focuses the beam in such a way that it later becomes collimated by another lens placed in front of the axicon. The beam from the other arm becomes slightly focused by this lens. A linear polarizer is used to regulate the intensities of the lasers in the combined beam. The axicon forms an accelerating Bessel beam with a cross section shown in the inset of Fig. 3.9 (the upper image shows the profile of the combined beam and the central and lower images are the profiles of its two frequency components). An aperture (a pinhole of about 1 μm diameter made in the center of a glass plate covered with a semi-transparent metal film) is placed after the axicon for creating a common-path interferometer. Due to the self-healing property of the Bessel beam, the plane-wave components propagate through the metal film and continue forming the accelerating Bessel beam. A part of the beam that propagates through the aperture is diffracted, forming a two-frequency spherical wave. We use this wave as a reference wave. The resulting interference between the accelerating Bessel beam and the reference wave is observed with a microscope objective and a camera. At a fixed position of the aperture, the microscope objective and the camera can be moved together along the axis, and the longitudinal interference pattern can be recorded.

The purpose of the common-path interferometer is to measure the phase distributions of the beam components [95]. In Publication IV, we have shown that the group velocity depends on the on-axis phase distributions of the beam components in accordance with $\frac{v_g}{c} = \frac{\varphi_1(z) - \varphi_2(z)}{\varphi_1^b(z) - \varphi_2^b(z)}$, where $\varphi_i = \omega_i z/c$ is the phase of the reference wave with frequency ω_i due to its propagation along the z-axis, and $\varphi_i^b(z)$ is the phase profile of component i of the Bessel beam along the beam axis. When the reference and sample fields are in phase, i.e., $\varphi_i^b(z_c) = \varphi_i(z_c)$, they show a constructive interference.

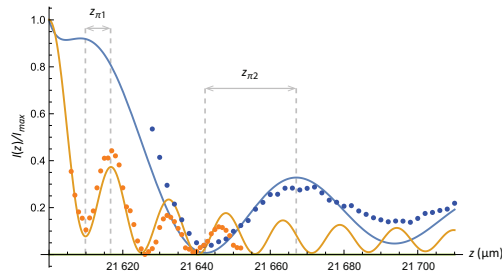

Figure 3.10. The measured longitudinal intensity profiles of the beam components interfering with reference waves. The wavelengths of the components are $\lambda_1 = 632.8$ nm (orange dots) and $\lambda_2 = 657.5$ nm (blue dots). The solid lines show fittings of the measured data with theoretical curves. The figure is adapted with permission from Publication IV © Optica Publishing Group.

Then, at a distance of $z_{\pi i}$ along the beam axis, for which we have $\varphi_i^{\mathrm{b}}(z_{\mathrm{c}} + z_{\pi i}) = \varphi_i(z_{\mathrm{c}} + z_{\pi i}) - \pi$, the interference is destructive. Hence, by measuring $z_{\pi i}$, for the two frequency components of the beam, we obtain the value of the local group velocity

$$v_{\mathrm{g}} = c\left(1 + \frac{1/z_{\pi 2} - 1/z_{\pi 1}}{2(1/\lambda_1 - 1/\lambda_2)}\right)^{-1}, \tag{3.12}$$

where $\varphi_i(z)$ is replaced with $2\pi z/\lambda_i$. An example of such a measurement is demonstrated in Fig. 3.10. The aperture is placed at a distance of 21.6 mm from the axicon tip and its sharp image is captured by the camera. Then, the microscope objective and the camera are moved away from the aperture in small steps, and the interference pattern is recorded for each frequency component of the Bessel beam. Each point on the plot represents the experimentally measured intensity value of the beam component (averaged over an area of 3×3 pixels in the central part of the beam). The solid lines are the fitting curves obtained by numerically superimposing a spherical wave with an expected Bessel beam:

$$I_j(z) = \left|\frac{c_{j1}\exp(ik_j z)}{z - z_0} + c_{j2}\exp\left(ik_j z\cos\alpha_j + i\phi\right)\right|^2, \tag{3.13}$$

where c_{j1}, c_{j2}, and ϕ are the fitting coefficients, z_0 is the origin of the spherical wave, k_j is the wavenumber, and α_j is the propagation angle of the plane-wave components of the Bessel beam formed by laser j. The distance $z_{\pi i}$ appears to be $z_{\pi 1} = 6.9$ μm for $\lambda_1 = 632.8$ nm and $z_{\pi 2} = 24.7$ μm for $\lambda_2 = 657.5$ nm.

To minimize possible errors, each measurement procedure described above is repeated 10 times. As a result, we obtain the mean value of $z_{\pi i}$ for each frequency component, $\overline{z_{\pi 1}} = 7.3$ μm and $\overline{z_{\pi 2}} = 25.4$ μm, together with their standard deviations, $\sigma_{\pi 1} = 0.48$ μm and $\sigma_{\pi 2} = 0.84$ μm. These values are used to calculate the average value of the measured group velocity as well as its lower v_{g}^- an upper v_{g}^+ limits

$$v_{\mathrm{g}}^{\pm} = c\left(1 + \frac{\dfrac{1}{\overline{z_{\pi 2}} \mp \sigma_{\pi 2}} - \dfrac{1}{\overline{z_{\pi 1}} \pm \sigma_{\pi 1}}}{2(1/\lambda_1 - 1/\lambda_2)}\right)^{-1}. \tag{3.14}$$

Thus, at a distance of 21.6 mm from the axicon tip, the group velocity of the accelerating Bessel beam is measured to be equal to approximately $5.6c$, with the lower and upper limits of $3.8c$ and $11.7c$, respectively. This and other measurement results are shown in Fig. 3.11. The solid blue line is given by Eqs. (3.8) and (3.11), representing a theoretical prediction of the group velocity behavior along the beam axis. The experimentally measured results are shown by the blue dots, and the corresponding error bars show the lower and upper limits of the measured group velocity. It

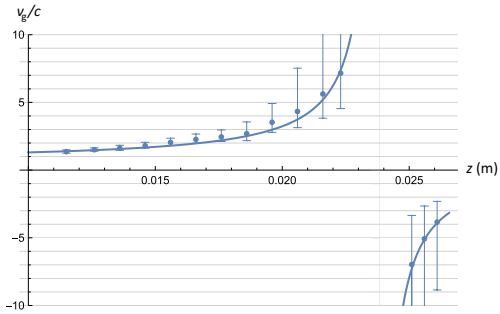

Figure 3.11. The measured group velocity of the longitudinally accelerating Bessel beam (see the blue dots and the estimated error bars). The blue line shows a theoretically predicted group velocity of the beam. The figure is adapted with permission from Publication IV © Optica Publishing Group.

can be seen that the group velocity is growing gradually from about $1.3c$ to infinity when approaching the discontinuity point at $z = 23.8$ mm, at which the denominator of Eq. (3.8) approaches zero. After this point, the group velocity changes its sign, staying infinite, and continues increasing towards zero. The highest group velocities that we were able to measure are $7c$ and $-7c$. The higher the magnitude of the group velocity is, the higher is the uncertainty of the measurement result. Therefore, the points close to the discontinuity of the curve were excluded from the plot.

As can be seen from Eq. (3.8), when the frequencies of the lasers are equal, the group velocity of the two-component Bessel beam is equal to zero as long as $\alpha_1 \neq \alpha_2$. This means that the intensity peaks do not move, forming a standing interference pattern. To generate such a Bessel beam, one of the lasers can be switched off, and the polarization plane of the other laser (e.g., with $\lambda_1 = 632.8$ nm) can be rotated by 45°. The collimated and focused components of the resulting Bessel beam will interfere and form a longitudinal standing-wave pattern that can be observed directly with the

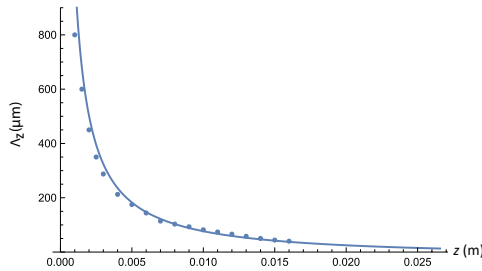

Figure 3.12. Measured period Λ_z of the longitudinal standing-wave pattern as a function of distance z from the tip of the axicon (blue dots). The solid line corresponds to the theoretically predicted dependence of Λ_z on z. The figure is adapted with permission from Publication IV © Optica Publishing Group.

camera. The period of this pattern can be calculated to be

$$\Lambda_z = \frac{2\pi}{k\,|\cos(\alpha_1) - \cos(\alpha_2)|}, \tag{3.15}$$

where k is the wave number of the laser. This function is shown by the solid blue line in Fig. 3.12. The blue dots show the experimentally measured values of the pattern period. At each coordinate z, the pattern period was measured by moving the camera in small steps and recording the transverse profile of the beam. Each value of the period was averaged over six measurements. The experimental results and the theoretical predictions are seen to be in a good agreement. The period decreases from 800 μm to 40 μm over a distance of 16 mm from the axicon tip.

If the lasers are swapped and their polarization planes are turned by 90°, the collimated and focused components of the Bessel beam have the wavelengths of $\lambda_1 = 657.5$ nm and $\lambda_2 = 632.8$ nm, respectively. The system with these parameters generates a longitudinally decelerating Bessel beam. The procedure of measuring the on-axis group velocity is the same as in the case of an accelerating Bessel beam. An example of a measurement at a coordinate $z = 12.5$ mm is demonstrated in Fig. 3.13. For the two components of the Bessel beam at the output of the common-path interferometer, we measured the distances $z_{\pi 1} = 12.5$ μm and $z_{\pi 2} = 19.6$ μm. After averaging these quantities over 10 measurements, we obtained $\overline{z_{\pi 1}} = 12.5$ μm, $\sigma_{\pi 1} = 0.71$ μm, $\overline{z_{\pi 2}} = 21.3$ μm, and $\sigma_{\pi 2} = 1.06$ μm. This gives for the group velocity an averaged value of $v_g = 0.78c$ and lower and upper limits of $0.75c$ and $0.82c$, as follows from Eq. (3.14). The comparison of the measured values of the on-axis group velocity and the theoretically predicted dependence of v_g on z is presented in Fig. 3.14. The blue dots and the corresponding error bars denote the experimental results, and the solid blue line is the calculated curve. The measured values of the group velocity agree well with the theoretically predicted results.

In summary, we have proposed and experimentally demonstrated continuous-wave and pulsed Bessel beams with a controllable (fixed or varying) group

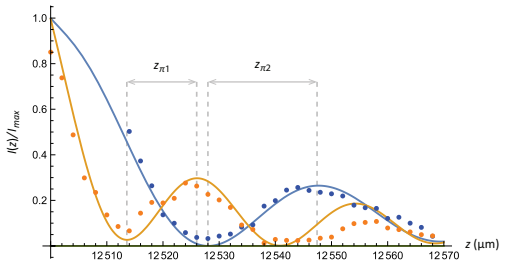

Figure 3.13. The measured longitudinal intensity profiles of the beam components interfering with reference waves. The wavelengths of the components are $\lambda_1 = 657.5$ nm (orange dots) and $\lambda_2 = 632.8$ nm (blue dots). The solid lines show fitting of the measured data with theoretical curves. The figure is adapted with permission from Publication IV © Optica Publishing Group.

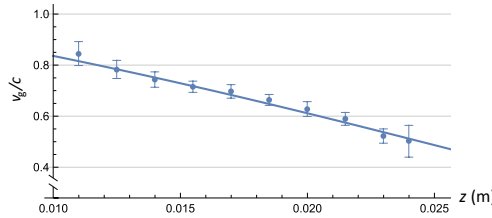

Figure 3.14. The measured group velocity of the longitudinally decelerating Bessel beam (see the blue dots and the estimated error bars). The blue line shows a theoretically predicted group velocity of the beam. The figure is adapted with permission from Publication IV © Optica Publishing Group.

velocity in free space. Subluminal, superluminal, negative, and zero group velocities were demonstrated using a single experimental setup. We have invented an interferometric method to measure group velocity through measuring the longitudinal phase distribution of the beam components. The obtained results are in good agreement with the theory. The proposed methods of controlling and measuring the group velocity can be applied to other types of optical beams and be of interest to scientists working in the fields of optical interferometry, ultrafast optics, nonlinear optics, and optical tweezers.

4. Conclusions

The focus of this dissertation is on the development of interferometric methods for imaging and detection as well as for creation of novel configurations of optical fields. We have utilized the coherence properties of light to demonstrate a novel interferometric imaging system that produces sharp images in the presence of severe aberrations. The method does not require any active compensation for the aberrations in contrast to methods of adaptive optics. Neither does it require time for transverse scanning and point-by-point correlation measurements between the sample and reference beams, in contrast to ghost imaging. Rather, it uses a spatially incoherent illumination with a relatively large longitudinal coherence length to make an unperturbed reference beam interfere with the aberrated sample beam and reveal the image of the object with a high transverse resolution. Our imaging method is independent of the type of aberration and is able to retrieve the image of the object after a fast processing of the recorded optical data. The experimental results show that even in the presence of strong aberrations, the retrieved image is not deformed and has a high resolution. The method was applied to create two different imaging systems, one based on a Mach-Zehnder interferometer to deal with transmissive objects, and the other is making use of a Michelson interferometer to image reflective objects. The method can be used for non-invasive imaging of microscopic objects hidden under a transparent scattering layer, such as a layer of biological or medical sample, and for compensating for significant focusing errors that can occur, for example, when scanning a three-dimensional object.

The aberrations that our imaging system is able to overcome should not shift the wavefront in the direction of the optical axis by a distance larger than the longitudinal coherence length of the light used. In principle, to increase the capabilities of the system, a microlens array can be used in addition to a microscope objective in the sample arm in order to increase the depth of field [96, 97]. This change should allow one to obtain high-quality images from a range of distances instead of a distance that is close to the focal length of the objective.

Another contribution of the thesis is a description of dynamic interference effects in multifrequency beating optical beams, which can be used to control the group velocity of light in free space. We have shown that by adjusting the propagation angles of the plane-wave components of a Bessel beam one can control the beam's group velocity and longitudinal acceleration. The acceleration can be obtained, for example, by transmitting a monochromatic Gaussian beam through a lens and an axicon. For pulsed and multifrequency cw Bessel beams, the group velocity can be adjusted rather freely, allowing one to obtain superluminal, subluminal, negative and zero group velocity, that can be made both fixed and varying in space and time. The thesis describes an experimental realization of a two-component cw Bessel beam with longitudinal acceleration and proposes a simple interferometric method for measuring the group velocity. The method is independent of the beam type and is based on the dependence of the group velocity on the on-axis phase distributions of the beam components. We have reliably measured the axial distribution of the group velocity with the values ranging from $-7c$ to $7c$. Optical beams with controlled group velocity can be of use in optical tweezers. For example, a pulsed or cw beam with a negative group velocity can be generated for trapping particles and moving them towards the light source. The zeroth-order Bessel beams considered in the thesis are beams with a very simple angular spectrum, which makes them attractive in view of the considered applications. However, the model can be extended to other types of optical beams, such as higher-order Bessel beams, light sheets, and hybrid Gaussian-Bessel beams, which can reveal new optical effects and lay the way for new applications.

The thesis mainly presents proof-of-concept studies with a large room for improvements. For example, the proposed method to measure the on-axis group velocity of an optical beam is an indirect method based on the measurement of the longitudinal phase distribution of the beam components. It would be useful to develop a direct measurement technique, for example, based on the detection of the intensity correlations using two-photon absorption [40, 98]. Furthermore, the setup can be modified to achieve extremely low values of group velocity, which could be beneficial for applications in optical tweezers. For this, the frequency components of the beam should be spectrally close to each other, which can be done by applying an acousto-optic phase shifter. The control of the group velocity of optical pulses can also be applied to compensate for the group velocity dispersion effects in a nonlinear medium, which can be used for pump-probe-type experiments in ultrafast optics.

References

[1] J. W. Goodman, *Statistical optics*. New York: Wiley, 2015.

[2] B. P. Abbott and *et.al.*, "Observation of gravitational waves from a binary black hole merger," *Phys. Rev. Lett.*, vol. 116, p. 061102, Feb 2016.

[3] R. L. Powell and K. A. Stetson, "Interferometric vibration analysis by wavefront reconstruction," *J. Opt. Soc. Am.*, vol. 55, pp. 1593–1598, Dec 1965.

[4] W. M. Macek and D. T. M. Davis, "Rotation rate sensing with traveling-wave ring lasers," *Applied Physics Letters*, vol. 2, no. 3, pp. 67–68, 1963.

[5] C. Magnain, A. Castel, T. Boucneau, M. Simonutti, I. Ferezou, A. Rancillac, T. Vitalis, J. A. Sahel, M. Paques, and M. Atlan, "Holographic laser doppler imaging of microvascular blood flow," *J. Opt. Soc. Am. A*, vol. 31, pp. 2723–2735, Dec 2014.

[6] D. Ausserré and M.-P. Valignat, "Wide-field optical imaging of surface nanostructures," *Nano Letters*, vol. 6, pp. 1384–1388, Jul 2006.

[7] A. Dubois, L. Vabre, R. Lecaque, and A.-C. Boccara, "Ultrahigh-resolution OCT using white-light interference microscopy," in *Coherence Domain Optical Methods and Optical Coherence Tomography in Biomedicine VII* (V. V. Tuchin, J. A. Izatt, and J. G. Fujimoto, eds.), vol. 4956, pp. 14 – 21, International Society for Optics and Photonics, SPIE, 2003.

[8] F. Zernike, "Phase contrast, a new method for the microscopic observation of transparent objects," *Physica*, vol. 9, no. 7, pp. 686–698, 1942.

[9] S. B. Mehta and C. J. Sheppard, "Using the phase-space imager to analyze partially coherent imaging systems: bright-field, phase contrast, differential interference contrast, differential phase contrast, and spiral phase contrast," *Journal of Modern Optics*, vol. 57, no. 9, pp. 718–739, 2010.

[10] Y. Peng, S. Choi, J. Kim, and G. Wetzstein, "Speckle-free holography with partially coherent light sources and camera-in-the-loop calibration," *Science Advances*, vol. 7, no. 46, p. eabg5040, 2021.

[11] B. E. A. Saleh and M. C. Teich, *Fundamentals of photonics; 2nd ed.* Wiley series in pure and applied optics, New York, NY: Wiley, 2007.

[12] F. Ferri, D. Magatti, V. G. Sala, and A. Gatti, "Longitudinal coherence in thermal ghost imaging," *Applied Physics Letters*, vol. 92, no. 26, p. 261109, 2008.

[13] L. Mandel and E. Wolf, *Optical Coherence and Quantum Optics*. Cambridge University Press, 1995.

[14] A. Shevchenko and T. Setälä, "Interference and polarization beating of independent arbitrarily polarized polychromatic optical waves," *Phys. Rev. A*, vol. 100, p. 023842, Aug 2019.

[15] R. A. Terborg, J. Pello, I. Mannelli, J. P. Torres, and V. Pruneri, "Ultrasensitive interferometric on-chip microscopy of transparent objects," *Science Advances*, vol. 2, no. 6, p. e1600077, 2016.

[16] K. L. Baker, "Interferometric wavefront sensors for high contrast imaging," *Opt. Express*, vol. 14, pp. 10970–10975, Nov 2006.

[17] R. Jones and C. Wykes, *Holographic and Speckle Interferometry*. Cambridge Studies in Modern Optics, Cambridge University Press, 2 ed., 1989.

[18] M. G. Genoni, S. Olivares, D. Brivio, S. Cialdi, D. Cipriani, A. Santamato, S. Vezzoli, and M. G. A. Paris, "Optical interferometry in the presence of large phase diffusion," *Phys. Rev. A*, vol. 85, p. 043817, Apr 2012.

[19] H.-L. Hsieh and P.-C. Kuo, "Heterodyne speckle interferometry for measurement of two-dimensional displacement," *Opt. Express*, vol. 28, pp. 724–736, Jan 2020.

[20] N. H. Wan, F. Meng, T. Schröder, R.-J. Shiue, E. H. Chen, and D. Englund, "High-resolution optical spectroscopy using multimode interference in a compact tapered fibre," *Nature Communications*, vol. 6, p. 7762, Jul 2015.

[21] J. W. Goodman, *Introduction to Fourier optics*. New York: McGraw-Hill, 3 ed., 2005.

[22] M. Born and E. Wolf, *Principles of Optics*. Cambridge University Press, 7 ed., 1999.

[23] T. Latychevskaia, "Lateral and axial resolution criteria in incoherent and coherent optics and holography, near- and far-field regimes," *Appl. Opt.*, vol. 58, pp. 3597–3603, May 2019.

[24] R. J. Zawadzki, S. M. Jones, S. S. Olivier, M. Zhao, B. A. Bower, J. A. Izatt, S. Choi, S. Laut, and J. S. Werner, "Adaptive-optics optical coherence tomography for high-resolution and high-speed 3d retinal in vivo imaging," *Opt. Express*, vol. 13, pp. 8532–8546, Oct 2005.

[25] R. E. Meyers, K. S. Deacon, and Y. Shih, "Turbulence-free ghost imaging," *Applied Physics Letters*, vol. 98, no. 11, p. 111115, 2011.

[26] G. R. Toker, *Holographic Interferometry A Mach–Zehnder Approach*. CRC Press, 1 ed., 2012.

[27] P. Xiao, M. Fink, and A. C. Boccara, "Full-field spatially incoherent illumination interferometry: a spatial resolution almost insensitive to aberrations," *Opt. Lett.*, vol. 41, pp. 3920–3923, Sep 2016.

[28] S.-H. Zhang, L. Gao, J. Xiong, L.-J. Feng, D.-Z. Cao, and K. Wang, "Spatial interference: From coherent to incoherent," *Phys. Rev. Lett.*, vol. 102, p. 073904, Feb 2009.

[29] A. M. Davis, S. A. Boppart, F. Rothenberg, and J. A. Izatt, *OCT Applications in Developmental Biology*, pp. 919–959. Berlin, Heidelberg: Springer Berlin Heidelberg, 2008.

[30] M. K. Kim, L. Yu, and C. J. Mann, "Interference techniques in digital holography," *Journal of Optics A: Pure and Applied Optics*, vol. 8, pp. S518–S523, jun 2006.

[31] V. Singh, S. Tayal, and D. S. Mehta, "Highly stable wide-field common path digital holographic microscope based on a fresnel biprism interferometer," *OSA Continuum*, vol. 1, pp. 48–55, Sep 2018.

[32] J. G. Fujimoto, W. Drexler, J. S. Schuman, and C. K. Hitzenberger, "Optical coherence tomography (oct) in ophthalmology: introduction," *Optics express*, vol. 17, March 2009.

[33] S. Mahajan, V. Trivedi, P. Vora, V. Chhaniwal, B. Javidi, and A. Anand, "Highly stable digital holographic microscope using sagnac interferometer," *Opt. Lett.*, vol. 40, pp. 3743–3746, Aug 2015.

[34] D. Wang, Y. Ning, A. Palmer, K. Grattan, and K. Weir, "An optical scanning technique in a white light interferometric system," *IEEE Photonics Technology Letters*, vol. 6, no. 7, pp. 855–857, 1994.

[35] J. C. Wyant, "The evolution of interferometry from metrology to biomedical applications," in *Quantitative Phase Imaging II* (G. Popescu and Y. Park, eds.), vol. 9718, pp. 1 – 13, International Society for Optics and Photonics, SPIE, 2016.

[36] B. L. Danielson and C. Y. Boisrobert, "Absolute optical ranging using low coherence interferometry," *Appl. Opt.*, vol. 30, pp. 2975–2979, Jul 1991.

[37] Z. Yang, L. Zhao, X. Zhao, W. Qin, and J. Li, "Lensless ghost imaging through the strongly scattering medium," *Chinese Physics B*, vol. 25, p. 024202, feb 2016.

[38] J. Dakin and R. Brown, *Handbook of Optoelectronics: Concepts, Devices, and Techniques Volume one (2nd ed.)*. Boca Raton, FL: CRC Press, 2017.

[39] J. H. Shapiro and R. W. Boyd, "The physics of ghost imaging," *Quantum Information Processing*, vol. 11, pp. 949–993, Aug 2012.

[40] A. Shevchenko, M. Roussey, A. T. Friberg, and T. Setälä, "Ultrashort coherence times in partially polarized stationary optical beams measured by two-photon absorption," *Opt. Express*, vol. 23, pp. 31274–31285, Nov 2015.

[41] A. Howie, J. E. Ffowcs Williams, J. E. Baldwin, and C. A. Haniff, "The application of interferometry to optical astronomical imaging," *Philosophical Transactions of the Royal Society of London. Series A: Mathematical, Physical and Engineering Sciences*, vol. 360, no. 1794, pp. 969–986, 2002.

[42] J. Davis, "Stellar angular diameter measurements by interferometry," in *Fundamental Stellar Properties: The Interaction Between Observation and Theory* (T. R. Bedding, A. J. Booth, and J. Davis, eds.), (Dordrecht), pp. 31–38, Springer Netherlands, 1997.

[43] T. Shirai, "Chapter one - modern aspects of intensity interferometry with classical light," vol. 62 of *Progress in Optics*, pp. 1–72, Elsevier, 2017.

[44] P. Hariharan and B. Sanders, "Ii quantum phenomena in optical interferometry," vol. 36 of *Progress in Optics*, pp. 49–128, Elsevier, 1996.

[45] A. Shevchenko, M. Roussey, A. T. Friberg, and T. Setälä, "Polarization time of unpolarized light," *Optica*, vol. 4, pp. 64–70, Jan 2017.

[46] G. J. Verbiest and M. J. Rost, "Beating beats mixing in heterodyne detection schemes," *Nature Communications*, vol. 6, p. 6444, Mar 2015.

[47] R. H. Kingston, "Optics and photonics," in *Optical Sources, Detectors, and Systems*, Optics and Photonics, p. ii, Burlington: Academic Press, 1995.

[48] J. Eichholz, D. B. Tanner, and G. Mueller, "Heterodyne laser frequency stabilization for long baseline optical interferometry in space-based gravitational wave detectors," *Phys. Rev. D*, vol. 92, p. 022004, Jul 2015.

[49] C. Greiner, B. Boggs, T. Wang, and T. W. Mossberg, "Laser frequency stabilization by means of optical self-heterodyne beat-frequency control," *Opt. Lett.*, vol. 23, pp. 1280–1282, Aug 1998.

[50] S. Hooker and C. Webb, *Laser Physics*. Oxford University Press, 2010.

[51] P. W. Milonni, *Laser physics*. Hoboken, NJ: John Wiley & Sons, 2nd ed., 2010.

[52] L. D. Landau and E. M. Lifshitz, *Electrodynamics of Continuous Media*. New York: Pergamon, 1984.

[53] J. P. Torres, M. Hendrych, and A. Valencia, "Angular dispersion: an enabling tool in nonlinear and quantum optics," *Adv. Opt. Photon.*, vol. 2, pp. 319–369, 2010.

[54] M. Yessenov, B. Bhaduri, P. J. Delfyett, and A. F. Abouraddy, "Free-space optical delay line using space-time wave packets," *Nature Communications*, vol. 11, p. 5782, Nov 2020.

[55] W. G. Brown, R. McLean, A. Sidorov, P. Hannaford, and A. Akulshin, "Anomalous dispersion and negative group velocity in a coherence-free cold atomic medium," *J. Opt. Soc. Am. B*, vol. 25, pp. C82–C86, Dec 2008.

[56] Z. A. Sabegh and M. Mahmoudi, "Superluminal light propagation in a normal dispersive medium," *Opt. Express*, vol. 29, pp. 20463–20476, Jun 2021.

[57] Z. Li and J. Kawanaka, "Optical wave-packet with nearly-programmable group velocities," *Communications Physics*, vol. 3, 2020.

[58] H. E. Kondakci and A. F. Abouraddy, "Airy wave packets accelerating in space-time," *Phys. Rev. Lett.*, vol. 120, p. 163901, Apr 2018.

[59] H. Kondakci and A. Abouraddy, "Optical space-time wave packets having arbitrary group velocities in free space," *Nature Communications*, vol. 10, 2019.

[60] M. A. Bandres and B. M. Rodríguez-Lara, "Nondiffracting accelerating waves: Weber waves and parabolic momentum," *New Journal of Physics*, vol. 15, p. 013054, jan 2013.

[61] P. Zhang, Y. Hu, T. Li, D. Cannan, X. Yin, R. Morandotti, Z. Chen, and X. Zhang, "Nonparaxial mathieu and weber accelerating beams," *Phys. Rev. Lett.*, vol. 109, p. 193901, Nov 2012.

[62] J. Zhao, P. Zhang, D. Deng, J. Liu, Y. Gao, I. D. Chremmos, N. K. Efremidis, D. N. Christodoulides, and Z. Chen, "Observation of self-accelerating bessel-like optical beams along arbitrary trajectories," *Opt. Lett.*, vol. 38, pp. 498–500, Feb 2013.

[63] I. Alexeev, K. Y. Kim, and H. M. Milchberg, "Measurement of the superluminal group velocity of an ultrashort bessel beam pulse," *Phys. Rev. Lett.*, vol. 88, p. 073901, Jan 2002.

[64] P. Bowlan, H. Valtna-Lukner, M. Lõhmus, P. Piksarv, P. Saari, and R. Trebino, "Measuring the spatiotemporal field of ultrashort bessel-x pulses," *Opt. Lett.*, vol. 34, pp. 2276–2278, Aug 2009.

[65] H. Valtna, K. Reivelt, and P. Saari, "Methods for generating wideband localized waves of superluminal group velocity," *Optics Communications*, vol. 278, no. 1, pp. 1–7, 2007.

[66] D. Giovannini, J. Romero, V. Potoček, G. Ferenczi, F. Speirits, S. M. Barnett, D. Faccio, and M. J. Padgett, "Spatially structured photons that travel in free space slower than the speed of light," *Science*, vol. 347, no. 6224, pp. 857–860, 2015.

[67] R. R. Alfano and D. A. Nolan, "Slowing of bessel light beam group velocity," *Optics Communications*, vol. 361, pp. 25–27, 2016.

[68] M. Yessenov and A. F. Abouraddy, "Accelerating and decelerating space-time optical wave packets in free space," *Phys. Rev. Lett.*, vol. 125, p. 233901, Dec 2020.

[69] C. J. Zapata-Rodríguez and M. A. Porras, "X-wave bullets with negative group velocity in vacuum," *Opt. Lett.*, vol. 31, pp. 3532–3534, Dec 2006.

[70] H. Valtna-Lukner, P. Bowlan, M. Lõhmus, P. Piksarv, R. Trebino, and P. Saari, "Direct spatiotemporal measurements of accelerating ultrashort bessel-type light bullets," *Opt. Express*, vol. 17, pp. 14948–14955, Aug 2009.

[71] M. Clerici, D. Faccio, A. Lotti, E. Rubino, O. Jedrkiewicz, J. Biegert, and P. D. Trapani, "Finite-energy, accelerating bessel pulses," *Opt. Express*, vol. 16, pp. 19807–19811, Nov 2008.

[72] D. McGloin and K. Dholakia, "Bessel beams: Diffraction in a new light," *Contemporary Physics*, vol. 46, no. 1, pp. 15–28, 2005.

[73] E. L. Dereniak and T. D. Dereniak, *Geometrical and Trigonometric Optics*. Cambridge University Press, 2008.

[74] J. Schwiegerling, "Theoretical limits to visual performance," *Survey of Ophthalmology*, vol. 45, no. 2, pp. 139–146, 2000.

[75] M. J. Booth, "Adaptive optical microscopy: the ongoing quest for a perfect image," *Light Sci. Appl.*, vol. 3, p. e165, 2014.

[76] A. J. Jesus-Silva, J. G. Silva, C. H. Monken, and E. J. S. Fonseca, "Experimental cancellation of aberrations in intensity correlation in classical optics," *Phys. Rev. A*, vol. 97, p. 013832, Jan 2018.

[77] T.-L. Kelly and J. Munch, "Phase-aberration correction with dual liquid-crystal spatial light modulators," *Appl. Opt.*, vol. 37, pp. 5184–5189, Aug 1998.

[78] E. Beaurepaire, A. C. Boccara, M. Lebec, L. Blanchot, and H. Saint-Jalmes, "Full-field optical coherence microscopy," *Opt. Lett.*, vol. 23, pp. 244–246, Feb 1998.

[79] T. Shirai, H. Kellock, T. Setälä, and A. T. Friberg, "Imaging through an aberrating medium with classical ghost diffraction," *J. Opt. Soc. Am. A*, vol. 29, pp. 1288–1292, Jul 2012.

[80] B. I. Erkmen and J. H. Shapiro, "Unified theory of ghost imaging with gaussian-state light," *Phys. Rev. A*, vol. 77, p. 043809, Apr 2008.

[81] R. S. Bennink, S. J. Bentley, and R. W. Boyd, ""two-photon" coincidence imaging with a classical source," *Phys. Rev. Lett.*, vol. 89, p. 113601, Aug 2002.

[82] A. Valencia, G. Scarcelli, M. D'Angelo, and Y. Shih, "Two-photon imaging with thermal light," *Phys. Rev. Lett.*, vol. 94, p. 063601, Feb 2005.

[83] D. S. Simon and A. V. Sergienko, "Correlated-photon imaging with cancellation of object-induced aberration," *J. Opt. Soc. Am. B*, vol. 28, pp. 247–252, Feb 2011.

[84] M. J. Padgett and R. W. Boyd, "An introduction to ghost imaging: quantum and classical," *Philosophical Transactions of the Royal Society of London A: Mathematical, Physical and Engineering Sciences*, vol. 375, no. 2099, 2017.

[85] N. D. Hardy and J. H. Shapiro, "Computational ghost imaging versus imaging laser radar for three-dimensional imaging," *Phys. Rev. A*, vol. 87, p. 023820, Feb 2013.

[86] S. Hartmann and W. Elsäßer, "A novel semiconductor-based, fully incoherent amplified spontaneous emission light source for ghost imaging," *Scientific Reports*, vol. 7, pp. 41866 EP –, Feb 2017. Article.

[87] A. F. Fercher, W. Drexler, C. K. Hitzenberger, and T. Lasser, "Optical coherence tomography - principles and applications," *Rep. Prog. Phys.*, vol. 66, p. 239, Jan 2003.

[88] B. Laude, A. D. Martino, B. Drévillon, L. Benattar, and L. Schwartz, "Full-field optical coherence tomography with thermal light," *Appl. Opt.*, vol. 41, pp. 6637–6645, Nov 2002.

[89] J. Durnin, "Exact solutions for nondiffracting beams. I. The scalar theory," *J. Opt. Soc. Am. A*, vol. 4, pp. 651–654, Apr 1987.

[90] T. Čižmár, M. Šiler, and P. Zemánek, "An optical nanotrap array movable over a milimetre range," *Applied Physics B*, vol. 84, pp. 197–203, Jul 2006.

[91] J. Turunen, A. Vasara, and A. T. Friberg, "Holographic generation of diffraction-free beams," *Appl. Opt.*, vol. 27, pp. 3959–3962, Oct 1988.

[92] J. Durnin, J. J. Miceli, and J. H. Eberly, "Diffraction-free beams," *Phys. Rev. Lett.*, vol. 58, pp. 1499–1501, Apr 1987.

[93] A. Shevchenko and T. Setälä, "Measurement of intensity and polarization beatings in the interference of independent optical fields," *Phys. Rev. Research*, vol. 2, p. 012053, Mar 2020.

[94] S. W. Jolly, O. Gobert, A. Jeandet, and F. Quéré, "Controlling the velocity of a femtosecond laser pulse using refractive lenses," *Opt. Express*, vol. 28, pp. 4888–4897, Feb 2020.

[95] H. Kadono, M. Ogusu, and S. Toyooka, "Phase shifting common path interferometer using a liquid-crystal phase modulator," *Optics Communications*, vol. 110, no. 3, pp. 391–400, 1994.

[96] K. Pang, L. Song, F. Fang, Y. Zhang, and H. Zhang, "An imaging system with a large depth of field based on an overlapped micro-lens array," *CIRP Annals*, vol. 65, no. 1, pp. 471–474, 2016.

[97] P.-Y. Hsieh, P.-Y. Chou, H.-A. Lin, C.-Y. Chu, C.-T. Huang, C.-H. Chen, Z. Qin, M. M. Corral, B. Javidi, and Y.-P. Huang, "Long working range light field microscope with fast scanning multifocal liquid crystal microlens array," *Opt. Express*, vol. 26, pp. 10981–10996, Apr 2018.

[98] A. Shevchenko, M. Roussey, T. Setälä, and A. T. Friberg, "Ultrafast polarization-state dynamics of light beams measured by two-photon absorption," in *Conference on Lasers and Electro-Optics*, p. SM2I.5, Optica Publishing Group, 2016.

Aalto-DT 32/2023

ISBN 978-952-64-1176-7 (printed)
ISBN 978-952-64-1177-4 (pdf)
ISSN 1799-4934 (printed)
ISSN 1799-4942 (pdf)

Aalto University
School of Science
Department of Applied Physics
www.aalto.fi

BUSINESS + ECONOMY

ART + DESIGN + ARCHITECTURE

SCIENCE + TECHNOLOGY

CROSSOVER

DOCTORAL THESES